1   **Modeling impacts of dust mineralogy on Earth's Radiation and Climate**

2

3   Qianqian Song[1], Paul Ginoux[2], María Gonçalves Ageitos[3,4], Ron L. Miller[5,6], Vincenzo Obiso[5],

4   Carlos Pérez García-Pando[4,7]

5   [1] Atmospheric and Oceanic Sciences Program, Princeton University, Princeton, NJ, USA

6   [2] NOAA Geophysical Fluid Dynamics Laboratory, Princeton, NJ, USA

7   [3] Projects and Construction Engineering Department. Universitat Politècnica de Catalunya-Barcelona

8   TECH, Terrassa, Spain

9   [4] Barcelona Supercomputing Center, Barcelona, Spain

10   [5] NASA Goddard Institute for Space Studies, New York, NY, USA

11   [6] Department of Applied Physics and Applied Mathematics, Columbia University, New York, NY, USA

12   [7] ICREA, Catalan Institution for Research and Advanced Studies, Barcelona, Spain

13   Correspondence: Qianqian Song (qs7080@princeton.edu)

Abstract

15 Mineralogical composition drives diverse dust impacts on Earth's climate systems. However, most
16 climate models still use fixed dust mineralogy, without accounting for its temporal and spatial
17 variation. To quantify the radiative impact of resolving dust mineralogy on Earth's climate, we
18 implement and simulate the distribution of dust minerals (i.e., illite, kaolinite, smectite, hematite,
19 calcite, feldspar, quartz, and gypsum) from Claquin et al. (1999) (C1999) in the GFDL AM4.0
20 model. Resolving dust mineralogy reduces dust absorption and results in improved agreement with
21 observation-based single scattering albedo (SSA), radiative fluxes from CERES (the Clouds and
22 the Earth's Radiant Energy System), and land surface temperature from CRU (Climatic Research
23 Unit), compared to the baseline bulk dust model version. It also results in distinct radiative impacts
24 on Earth's climate over North Africa. Over the 19-year (from 2001 to 2019) modeled period during
25 JJA (June-July-August), it leads to a reduction of over 50% in net downward radiation across the
26 Sahara and approximately 20% over the Sahel at top of atmosphere (TOA). The reduced dust
27 absorption weakens the atmospheric warming effect of dust aerosols and leads to an alteration in
28 land surface temperature, resulting in a decrease of 0.4K over the Sahara and an increase of 0.6K
29 over the Sahel. The less warming in the atmosphere suppresses ascent and weakens the monsoon
30 inflow from the Gulf of Guinea. This brings less moisture to the Sahel, which combined with
31 decreased ascent induces a reduction of precipitation. Interestingly, we find similar results by
32 simply fixing the hematite content of dust to 0.9% by volume, which is more computationally
33 efficient than simulating all minerals. However, uncertainties related to emission and distribution
34 of minerals may blur the advantages of resolving minerals to study their impact on radiation, cloud
35 properties, ocean biogeochemistry, air quality, and photochemistry. On the other hand, lumping
36 together clay minerals (i.e., illite, kaolinite, and smectite), but excluding externally mixed hematite
37 and gypsum, appears to provide both computational efficiency and relative accuracy. Nevertheless,
38 for specific research, it may be necessary to fully resolve mineralogy to achieve accuracy.

1   Introduction

40 Soil dust aerosols emitted from erodible land surfaces, hereafter referred to as dust, are the most
41 abundant aerosol component in the atmosphere in terms of dry mass. Dust has significant impacts on
42 the Earth's climate systems (atmosphere, ocean, cryosphere) due to its interaction with terrestrial and
43 solar radiation (Sokolik and Toon, 1999), cloud microphysics (Guo et al., 2021), tropospheric

44   chemistry (Bian and Zender, 2003; Paulot et al., 2016), and oceanic and terrestrial

45   biogeochemistry(Mahowald, 2011; Evans et al., 2019; Dunne et al., 2020). In addition, dust particles

46   deposited on snow and ice decrease surface reflectivity and accelerate snowmelt (Skiles et al., 2018;

47   Réveillet et al., 2022). Dust can influence Earth's radiative energy budget through different pathways;

48   among them: 1) directly by interacting with both solar and terrestrial radiation (i.e., direct radiative

49   effects, hereafter referred to as DRE) 2) by radiatively influencing the thermal dynamical structure of

50   atmosphere and thereby clouds (i.e., semi-direct radiative effect) and 3) indirectly by altering cloud

51   reflectivity (cloud albedo effect) and lifetime (cloud lifetime effect). Unfortunately, the quantitative

52   estimate of dust DRE at the top of atmosphere (TOA) is largely uncertain (Claquin et al., 1998; Miller

53   et al., 2014; Kok et al., 2017; Song et al., 2022). A significant part of this uncertainty has been attributed

54   to neglecting variations in dust mineralogical composition and its evolution during transport (Li et al.,

55   2021).

56   The magnitude of dust impacts on the Earth's climate systems depends on its mineralogical

57   composition, as has been shown in multiple studies. In the ShortWave (SW), dust absorption depends

58   on the iron oxides content. Sokolik and Toon (1999) suggested that a small amount of iron oxides

59   internally mixed with less absorptive minerals is able to reverse the sign of DRE_{SW} at TOA from

60   negative (cooling effect) to positive (warming effect). Multiple studies have confirmed the importance

61   of iron oxides to the dust DRE_{SW} (Balkanski et al., 2007; Li et al., 2021; Obiso et al., 2023). In

62   LongWave (LW) spectrum, absorption and DRE_{LW} depend on the abundance of quartz, calcite, and

63   clays in coarse and super-coarse modes (Di Biagio et al., 2017; Sokolik and Toon, 1999). As a result,

64   resolving dust mineralogy allows to better understand the impact of dust DRE, such as the fast response

65   (i.e., the response with fixed sea surface temperature) of the Earth's surface radiation (Persad et al.,

66   2014), land surface temperature, precipitation (Ming et al., 2010), and atmospheric circulation. Dust

67   absorption can also affect the slow climate response (i.e., the response including changes in sea surface

68   temperature) of the Earth surface temperature (Miller and Tegen, 1998), precipitation, ocean heat

69   transport (Ocko et al., 2014), which may affect hurricane genesis (Strong et al., 2018), and induce

70   feedback (Miller et al., 2004; Miller et al., 2014).

71   In addition, resolving dust mineralogy is also crucial for studying heterogeneous reactions of acid gases

72   with dust aerosols. For example, the uptake of HNO_3, NO_3^-, N_2O_5 on dust particles is suggested to be

73   limited by alkalinity that comprises calcium and magnesium carbonates (Song and Carmichael, 2001;

74   Paulot et al., 2016). These reactions will modify the composition of dust particles and subsequently

75   changing their hygroscopicity, cloud condensation nucleation (CCN), and ice nucleation activities

76   (Kelly et al., 2007), and thereby further affecting precipitation (Rosenfeld et al., 2001). Moreover,

77   heterogeneous reactions with mineral dust could significantly affect tropospheric photochemical

78   oxidation cycles, causing up to 10% reduction in O3 concentrations in dust source regions and nearby

79   (Dentener et al., 1996). Among the different minerals, K-Feldspar appears to dominate ice nucleation,

80   despite being a minor component of aeolian dust (Atkinson et al., 2013; Harrison et al., 2019), although

81   other minerals such as quartz may also contribute (Chatziparaschos et al., 2023). The key factor

82   controlling the production and removal of pollutants and the damages by acid rain is the pH of

83   raindrops, which has been observed to increase due to its dependency on Ca-rich dust (Grider et al.,

84   2023).

85   Despite the potential importance of resolving dust mineralogy in various aspects, current climate

86   models tend to use a fixed mineralogy without considering the temporal and spatial variations in

87   dust mineralogical composition. To test the importance of resolving dust mineralogy on the fast

88   climate response (e.g., surface temperature response over land, atmospheric circulation and

89   precipitation response) through its interactions with SW and LW radiation (i.e., through dust DRE),

90   dust mineralogy has been implemented and simulated in the GFDL AM4.0 model (Zhao et al.,

91   2018a, b), including its on-line interactions with radiation. Following the pioneering work of

92   Claquin et al. (1999) (C1999), we consider the emission, transport and interactions with radiation

93   and deposition of eight minerals: illite, kaolinite, smectite, hematite, calcite, feldspar, quartz and

94   gypsum. Following the recent launch of the Earth Surface Mineral Dust Source Investigation

95   (EMIT) instrument specifically designed to retrieve global distribution of dust mineralogy over

96   dust sources (Green et al., 2020), there have been coordinated efforts to represent dust mineralogy

97   in climate models, in particular in Li et al. (2021), Gonçalves Ageitos et al. (2023), and Obiso et

98   al. (2023). Our work joins these efforts, with the additional focus on studying the fast climate

99   response of resolving dust mineralogy to dust DRE. The impacts of dust mineralogy on other

100   aspects, such as heterogeneous reactions and ice nucleation ability, will be examined in future

101   studies. Section 2 provides the description of the GFDL AM4.0 model and dust mineralogy

102   implementation. Section 3 describes our experimental design. In Section 4, we calculate mineral

103   optical properties, activate the interaction of minerals with radiation in GFDL AM4.0 and compare

104   modeled dust optical properties with observations. Section 5 presents the impacts of resolving dust

105   mineralogy on Earth's radiation and climate with a focus on the North Africa, as well as their

106 evaluations. In Section 6, we investigate the influences of reducing the number of mineral tracers.

107 Section 7 provides a summary of the study along with the main conclusions.

2   Model and Data

2.1   Model description

110 We conduct a series of Atmospheric Model Intercomparison Project (AMIP; Gates, 1992)

111 experiments with GFDL AM4.0 (Zhao et al., 2018a, b) over the period 2001-2019. Observed

112 gridded SST and sea‑ice concentration boundary conditions are from the reconstructions of Taylor

113 et al., (2000). Historical reconstructions of monthly solar spectral irradiances are from Matthes et

114 al., (2017). For radiation calculations, global monthly mean concentrations of greenhouse gases

115 (GHGs), including nitrous oxide (N_2O), and ozone‑depleting substances (ODSs, including CFC-

116 11, CFC‑12, CFC‑113, and HCFC‑22) are specified from Meinshausen et al., (2017). The solar

117 irradiances and GHG databases are standard for CMIP6.

118 In AM4.0, dust emission is calculated interactively following the parameterization of Ginoux et al.

119 (2001) with a threshold of wind erosion and global scaling factor of 3.5 $m\ s^{-1}$ and 0.2 $\mu g\ s^2\ m^{-5}$,

120 respectively. Dust size is represented by five bins with diameter ranging from 0.2 μm to $20\mu m$,

121 with updated values of 0.04, 0.14, 0.19, 0.49, and 0.14 for the corresponding source fractions. Dust

122 mineral composition is considered as uniform, with no temporal and spatial variations; in other

123 words, dust Refractive Index (RI) is temporally and spatially homogeneous (case referred to as

124 homogeneous dust hereafter). The dust RI in the standard AM4.0 is taken from Balkanski et al.,

125 (2007), assuming a fixed hematite content of 2.7% by volume (HD27), which is calculated for the

126 internal mixture of hematite and five other minerals (calcite, quartz, illite, kaolinite and

127 montmorillonite) using a Maxwell-Garnet mixing rule. The control run conducted with the

128 standard AM4.0 model is labeled as HD27 as described in Table 2.

129 In addition, we conduct simulations assuming homogeneous dust with hematite content of 0.9%

130 by volume, with RI from Balkanski et al. (2007). Similar to HD27, this experiment, labeled as

131 HD09 in Table 2, does not account for the temporal and spatial variations in dust mineralogy.

2.2 Dust mineralogy implementation

132

133   Claquin et al. (1999) (C1999) is the earliest study providing a soil mineralogy map oriented toward

134   atmospheric and climate modelling. The soil map provides the mineral mass fractions present in

135   the clay and silt size ranges for eight different minerals, namely: illite, smectite, kaolinite, calcite,

136   quartz, feldspars, gypsum, and hematite. In this study, we implement the eight minerals from the

137   soil map provided by C1999, in GFDL AM4.0 to resolve dust (for more details see Ginoux et al.

138   2023, in preparation). The soil map is based on soil analyses that are usually done after wet sieving,

139   which disperse mineral aggregates into small particles. We apply an algorithm based on Brittle

140   Fragmentation Theory (BFT; Kok, 2011) to reconstruct the mineral aggregates emitted from the

141   original undispersed soils. The mass density of the eight minerals, along with a brief description

142   of their importance to Earth's climate, are listed in Table 1. The density of minerals impacts their

143   settling velocity, which is relevant to the removal of particles in the atmosphere. Iron oxides,

144   represented by hematite in C1999, have larger density than other minerals, so that hematite

145   deposits more quickly and is not able to be transported to remote regions when not aggregated or

146   internally mixed with lighter clay minerals. Moreover, hematite is the strongest absorber in the

147   visible. As such, the correct representation of hematite content in dust aerosols is critical in

148   improving the representation of dust interaction with SW radiation in climate models. Considering

149   that iron oxides are usually found as accretions in other minerals, particularly phyllosilicates (clay

150   minerals): illite, kaolinite and smectite (Zhang et al., 2015; Panta et al., 2023), we partition

151   hematite into two portions: internally mixed hematite and externally mixed hematite, in terms of

152   their mixing state with clay minerals. For accretions, we take the 5% mass fraction of hematite in

153   the mixture at emission as a reference to estimate the amount of internally mixed hematite

154   (following Gonçalves Ageitos et al., 2023). Specifically, hematite is internally mixed with clay

155   minerals for the portion of its mass fraction at emission that is less than 5%, while it is considered

156   externally mixed for the portion that exceeds 5%.

157   In addition to the similar roles of clay minerals in carrying iron oxides, the optical properties of

158   the three clay minerals are very similar, and their optical properties of the external mixture is found

159   to be almost identical to their internal mixture (see Section S1 in the Supplement). This finding

160   implies that we could use a single mineral species to represent all three clay minerals in their

161   interaction with radiation to reduce computational cost. Therefore, the optical properties of one

162   single mineral (clay433, see descriptions in Supplementary Section S1) are used to represent the

163 optical properties of all three clay minerals. This simplifies the calculations of optical properties

164 for internal mixtures of hematite and three clay minerals, reducing it from an internal mixture of

165 four minerals (hematite, illite, kaolinite and smectite) to an internal mixture of two minerals

166 (hematite and clay433).

167 The optical properties of the internal mixture of hematite and clay433 are calculated using three

168 mixing rules: volume weighted average (VOL-mixing), Maxwell-Garnett mixing rule (MG-

169 mixing) and Bruggeman mixing rule (BM-mixing). These calculations are performed for various

170 volume mixing fractions of hematite with respect to clay433, to construct a lookup table for each

171 mixing rule. The optical properties of each mineral as well as the internal mixtures of hematite and

172 clay433 are calculated offline using Mie code with a spherical shape assumption. As all other

173 minerals have similar SW absorption, internal or external mixing does not change their absorption

174 properties. So, we assume all other minerals to be externally mixed.

175 Overall, we implement nine types of mineral tracers: seven non-hematite minerals along with

176 distinguished internal and external hematite, as listed in Table 1. Each type is distributed across

177 five size bins. As a result, 45 mineral tracers have been incorporated in AM4.0 to account for dust

178 mineralogy.

179 Table 1. The list of minerals considered in this study and their importance to Earth's climate. Mineral-
180 dependent mass densities are defined following Table 1 in Gonçalves Ageitos et al. (2023), in which the
181 references of mineral densities are listed.

Minerals	Density (kg/m^3)	Importance
1. Hematite (int.)	2570	It is the strongest visible absorber. It is internally mixed with clay minerals when its mass fraction at emission < 5%.
2. Hematite (ext.)	4770[1]	It is externally mixed for the part of emitted mass fraction > 5%.
Three clay minerals: 3. Illite 4. Smectite 5. Kaolinite Clay in BM-RT	2570 2570 2630 2590	They are the most abundant mineral components in clay-sized (diameter $< 2\mu m$) minerals. They are internally mixed with internal hematite. The three clay minerals are lumped together as one mineral species 'clay' in the BM-RT experiment in Section 6.
6. Calcite	2710	It is important for chemistry. (e.g., heterogeneous reaction with acidic gases and formation of sulfate and nitrates on the surface of dust particles, and cloud droplet pH)

7. Feldspar	2680	A fraction of feldspar (K-feldspar) is important for ice nucleation
8. Quartz	2670	It is the most abundant mineral component in silt-sized (diameter:2-63 μm) minerals. It is important for LW absorption and ice nucleation.
9. Gypsum	2308	It possibly has impact on chemistry, but the impact is likely unimportant given the low abundance globally.

[1] We use the mean of hematite and goethite densities for hematite, as in Gonçalves Ageitos et al. (2023).

2.3 AERONET Dust SSA

The AERONET Version 3 Level 2.0 Almucantar retrievals (Giles et al., 2019; Sinyuk et al., 2020) from 2000 to 2020 are screened for dust events following the methodology in Gonçalves Ageitos et al. (2023) and Obiso et al. (2023). This screening process aims to select dust-dominated events and filter out the AERONET scenes contaminated by other absorbing aerosols. The criteria that are applied to AERONET retrievals to screen dust events are: 1) hourly retrievals from AERONET are considered to represent dust when the fine volume fraction is small (below 15%), 2) the SSA increases from 440 nm to 675 nm (a feature that distinguishes dust from other species, see Dubovik et al., 2002), and 3) the mean of the imaginary index at red and near-infrared wavelengths (675, 870 and 1020 nm) is lower than 0.0042 (as higher values would indicate the presence of absorbing black and brown carbon, following Schuster et al., 2016). We calculate AERONET SSA in the visible by averaging AERONET retrieved SSA at two visible wavelengths (0.44 μm and 0.67 μm) weighted by solar spectrum.

2.4 Laboratory Dust SSA

The lab measured dust SSA at 550 nm is obtained from Di Biagio et al. (2019) (DB-2019 hereafter), in which dust SSA was directly retrieved from scattering and absorption measurements. We acknowledge the limits of laboratory measurements, where the dust samples are not aerosols present in the atmosphere, but instead are reemitted in the lab from soil samples collected from various source regions. Consequently, the laboratory measurements in DB-2019 do not account for dust aerosols transported from other regions to the regions of interest. In addition, in contrast to the modeled dust diameter range of 0.2 μm to $20\mu m$, DB-2019 measures dust particles with a diameter ranging from 0.2 μm up to $10\mu m$.

2.5 CERES Data

To compare modeled fluxes at TOA with observations, we use the Clouds and the Earth's Radiant Energy System (CERES) Energy Balanced and Filled (EBAF) Edition-4.2 data (Loeb et al., 2018). The standard CERES level-3 products provide clear-sky fluxes by averaging all CERES footprints within a region that are completely free of clouds. Therefore, there are many missing regions in monthly mean clear-sky TOA flux maps because completely cloud-free conditions are not always observed at the CERES footprint scale (~20 km at nadir). In contrast to the standard CERES level-3 products, CERES_EBAF product infers clear-sky fluxes from clear portions of partly cloudy CERES footprints thereby producing a clear-sky TOA flux climatology free of any missing regions (details in Loeb et al., 2018). Starting from CERES_EBAF_Ed4.1, the product also provides clear-sky flux estimates for the total region (i.e., the total CERES footprints) by combining CERES observations and radiative transfer calculations, which represents clear-sky flux with clouds removed from the entire atmospheric column of CERES footprints. These clear-sky fluxes for the total region are defined in a way that is more consistent with how clear-sky fluxes are represented in climate models (for details see CERES_EBAF_Ed4.1 Data Quality Summary). In this study, the monthly mean TOA 'Clear-Sky Flux Estimate for Total Region' variables in the CERES_EBAF_Ed4.2 product, the most recent version of the product, are used to compare with modeled monthly mean clear-sky flux at TOA. The comparisons allow us to examine the agreement of modeled clear-sky fluxes from different experiments with observations. The comparison results will be shown in section 5.1.

2.6 CRU TS Data

The CRU TS (Climatic Research Unit gridded Time Series) dataset provides high-resolution (0.5° latitude × 0.5° longitude) climate dataset over land except Antarctica. The dataset is based on extensive networks of weather stations going back to 1901(Harris et al., 2020). This dataset has been widely used in various research areas since its first release in 2000. The mean 2-meter temperature (TMP) and precipitation rate (PRE) variables from CRU TS v4.07 are used to evaluate our model simulations. The results will be shown in section 5.2 and section 5.3.

3 Experimental Design

Table 2. List of experiments and their description. Experiments are named based on the type of dust used or the mixing rules for minerals applied in each experiment.

Experiments	Dust or Minerals	Description	Optics
HD27	HD27	Dust refractive index is spatially and temporally uniform. Dust is assumed to contain 2.7% of hematite by volume. Its optical properties are used to represent dust in the standard GFDL AM4.0 model.	Balkanski et al. (2007)
HD09	HD09	Dust refractive index is spatially and temporally uniform. Dust is assumed to contain 0.9% of hematite by volume.	Balkanski et al. (2007)
VOL	VOL-mixing	Soil mineralogy from C1999 is implemented in AM4.0. Hematite (int.) is internally mixed with clay minerals following the volume-weighted mean mixing rule.	Scanza et al. (2015)
MG	MG-mixing	Soil mineralogy from C1999 is implemented in AM4.0. Hematite (int.) is internally mixed with clay minerals following the Maxwell Garnett mixing rule.	Scanza et al. (2015)
BM	BM-mixing	Soil mineralogy from C1999 is implemented in AM4.0. Hematite (int.) is internally mixed with clay minerals following the Bruggeman mixing rule.	Scanza et al. (2015)
BM-RT	BM-mixing	Three experiments are performed step by step to reduce the number of mineral tracers. 1) BM-LC experiment: following BM experiment, illite, kaolinite and smectite are lumped together as one tracer 'clay'. 2) BM-LCRH experiment: following BM-LC, external mixed hematite is further removed, its mass is combined with internal mixed hematite. 3) BM-LCRHRG experiment: following BM-LCRH, gypsum is further removed, and its mass is proportionally added to all other remaining minerals.	Scanza et al. (2015)

We conduct a total of six experiments using the GFDL AM4.0 model, with each experiment's description provided in Table 2. Two of these experiments serve as control runs in which dust aerosols are represented with temporally and spatially fixed composition in the model. The first control run, referred to as HD27, represents how dust aerosols are implemented in the standard GFDL AM4.0 model (Zhao et al., 2018a). The second control run is the HD09, in which dust is more scattering than that in the standard AM4.0 model (i.e., HD27) due to its reduced hematite volume fraction from 2.7% to 0.9%.

241 The other three experiments, namely VOL, MG, and BM, resolve dust mineralogy and activate

242 their interaction with radiation. These three experiments incorporate 45 mineral tracers for nine

243 types of mineral tracers distributed over five size bins. Additionally, we conduct the BM-RT

244 experiments, which consist of three sub-experiments: BM-LC, BM-LCRH, BM-LCRHRG. These

245 experiments aim to explore the potential of reducing mineral tracers, which can improve the model

246 computational efficiency. The results will be discussed in Section 6.

247 Each of the experiments ran for 19 years, from 2001 to 2019. We consider the 19-year runs of the

248 experiment as a group of simulations, containing 19 members of one-year simulation. The two

249 control runs (i.e., HD27 and HD09), combined with the three mineral-resolved experiments (i.e.,

250 VOL, MG, and BM), form a total of six contrasting pairs. In this study, we define the anomaly as

251 the group mean difference (based on 19-year mean) between mineral-resolved experiment and

252 control run for each contrasting pair. An anomaly is considered statistically significant if the p-

253 value from the student's t-test is smaller than 0.05.

254 4 Optical Properties

255 4.1 Dust optical properties
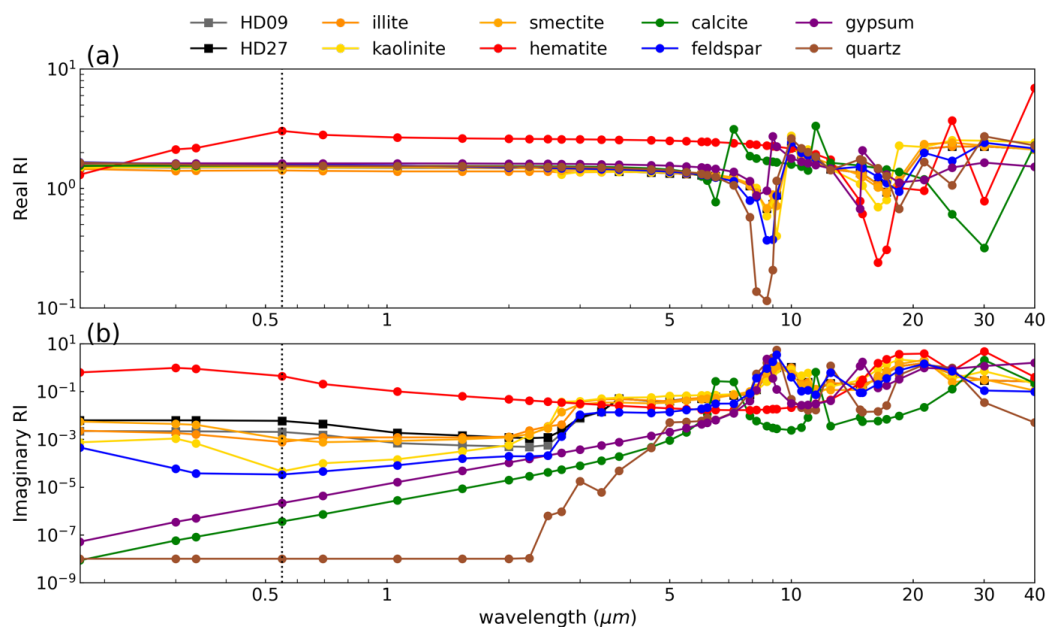
256

257 Figure 1. Real part and imaginary part of complex refractive indices (RI) of two homogeneous dust (i.e.,
258 HD27 and HD09) and eight minerals (Scanza et al., 2015).

259   Figure 1 shows the refractive indices (RI) of each mineral (Scanza et al., 2015) as well as the RI

260   of two homogeneous dust mixtures HD27 and HD09 (Balkanski et al., 2007). The HD09 dust has

261   lower imaginary part of RI at 550 nm than HD27 dust, indicating its lower absorption in the visible

262   band due to a reduced content of hematite.

263   With the optical properties of each mineral component calculated in Section 2.2, we incorporate

264   the interaction of minerals with radiation into GFDL AM4.0. Table 3 provides the global total dust

265   emission, load, globally averaged dust aerosol optical depth (DAOD) and SSA for each experiment

266   listed in Table 2. DAOD and SSA from AM4.0 simulations are averaged in the visible band (0.44-

267   0.625μm) of GFDL AM4.0. Note that in our calculations, the domain averaged DAOD is always

268   weighted by the area of each grid cell. The domain averaged SSA is always weighted by the area

269   and DAOD of each grid cell. Additionally, the spectral-averaged DAOD and SSA are always

270   weighted by solar spectrum, which peaks at around 0.50 μm. The emission, load, deposition, and

271   lifetime for each mineral are provided in Table S1 in the Supplement. The subtle difference in

272   DAOD and large variation in dust SSA across experiments suggests that resolving dust mineralogy

273   or changing hematite content in homogeneous dust does not affect visible extinction of dust

274   aerosols (i.e., DAOD). However, it significantly affects the relative strength of dust absorption

275   versus scattering. The variation in total dust emission and DAOD across different experiments

276   results from the feedback of dust interactions with radiation (Miller et al., 2004; Pérez et al., 2006;

277   Miller et al., 2014), which is influenced by the distinct scattering properties of dust aerosols in

278   each experiment. The HD27 dust used in the standard AM4.0 model is the most absorptive among

279   all experiments. The HD09 dust is much less absorptive due to its smaller hematite content, thereby

280   resulting in a lower imaginary part of RI in the visible range (Figure 1). We can see that the SSA

281   of HD09 dust is very similar to the values obtained in cases where minerals are resolved (i.e., MG

282   and BM). For the three mineral-resolved experiments, the lower global mean SSA in VOL suggests

283   that VOL-mixing dust is more absorptive than MG-mixing and BM-mixing dust. This finding is

284   consistent with previous studies that have suggested that VOL-mixing method, when applied to

285   minerals to compute the bulk aerosol optical properties, may artificially enhance absorption

286   relative to scattering and lead to a lower SSA for bulk dust aerosol (Zhang et al., 2015).

287   Table 3. 19-year (2001-2019) averaged global dust emission, load, globally averaged visible band dust
288   optical depth (DAOD) and single scattering albedo (SSA) for each experiment in this study. We use each
289   grid-cell surface area as a weight for the global DAOD average. We use each grid-cell surface area times
290   DAOD in each grid-cell as a weight for the global SSA average. In addition, we include the results from

291   previous studies for the purpose of comparison. Note, the modeled DAOD and SSA in this study are
292   averaged in the visible band (0.44 – 0.625μm) of GFDL AM4.0, while averaged in the UV-VIS band (0.30
293   – 0.77μm) of GISS ModelE2.1 in Obiso et al. (2023).

Experiments			Emission (Tg/yr)	Load (Tg)	DAOD	SSA
HD27			3354	23.6	0.023	0.86
HD09			3119	21.5	0.020	0.93
VOL			3154	21.6	0.022	0.91
MG			3083	21.1	0.021	0.93
BM			3087	21.1	0.021	0.93
BM-RT	BM-LC		3097	21.1	0.021	0.930
	BM-LCRH		3069	20.9	0.021	0.930
	BM-LCRHRG		3110	21.4	0.021	0.928
AeroCom [1]			1123 (500 – 4400)	15.8 (7-30)	0.023 (0.01 - 0.053)	-
GISS ModelE2.1 [2]	HOM		4031	31.3	0.020	0.917
	EXT		4152	32.4	0.020	0.936
	INT		4284	33.7	0.021	0.942

(1) Results based on 15 global aerosol models within the AeroCom project (Huneeus et al., 2011).

(2) Results from Obiso et al. (2023).

4.2   Comparison of dust optical properties with observations

295   Iron oxides content of dust determines shortwave radiation absorption by dust: the higher amount
296   of iron oxides, the lower the SSA. Following our calculations of dust optical properties in Section
297   4.1, we compared GFDL AM4.0 modeled dust SSA (averaged in the visible band 0.44-0.625 μm)
298   against AERONET SSA retrievals (averaged at two visible wavelength: 0.44 μm and 0.67 μm) in
299   Section 4.2.1 and laboratory measurements of SSA (at 0.55 μm) in Section 4.2.2. The modeled
300   dust SSA is evaluated with observation-based results utilizing three evaluation metrics: The
301   standard deviation (σ), derived from SSA for all locations displayed in Figure 2, is used as an
302   indicator of dust SSA spatial variation. The normalized mean bias (nMB) and normalized root
303   mean square error ($nRMSE$) are utilized to assess the mean bias and root mean square error,

13

304   respectively, of modeled SSA in comparison to observed SSA. Definitions of nMB and $nRMSE$

305   are provided in Section S2 in the Supplement.

4.2.1   Comparison with AERONET retrievals

307   Figure 2 displays the AERONET stations selected by filtering dust events. Figure 3a shows GFDL

308   AM4.0 modeled 19-year (2001-2019) averaged dust SSA (average in 0.44-0.625 μm) versus

309   AERONET SSA (average at 0.44 μm and 0.67 μm) retrievals. Compared to AERONET SSA

310   retrievals, both HD27 and VOL overestimate dust absorption, as indicated by their relatively low

311   SSA (Figure 3a). HD27 dust is the most absorptive, indicating that the standard AM4.0 dust is

312   overly absorptive. Dust SSA in MG and BM are quite similar (i.e., mean SSA: 0.926 versus 0.927)

313   and show a better agreement with AERONET measurements ($nMB \approx -1.3\%$ and $nRMSE \approx$

314   1.6%), and they exhibit stronger scattering (i.e., higher SSA) than HD27 and VOL. HD09 is almost

315   as scattering as MG and BM, as indicated by the mean SSA of 0.929 versus 0.926 and 0.927 in

316   Figure 3a, which is consistent with the global mean SSA results shown in Table 3. Overall, both

317   the fixed mineralogy dust HD09 and mineral-resolved MG and BM dust agree well with

318   AERONET SSA retrievals, while HD27 and VOL are too absorptive.

319   We further assess the SSA spatial variation (indicated by σ) for each experiment from AM4.0 by

320   comparing it to observation-based results. SSA is generally determined by dust mineralogy, size

321   as well as shape. various dust mineralogy leads to distinct dust SSA due to the different absorption

322   properties of minerals (Figure 1). Coarser dust generally tends to be more absorptive (i.e., has

323   lower SSA) than finer dust when other factors are the same (Ryder et al., 2018). Spherical dust

324   assumption tends to underestimate dust SSA (Huang et al., 2023). Given the uncertainty in dust

325   shape, we assume dust particles to be spherical in this study, aligning with other model studies

326   (e.g. Gliß et al., 2021). Consequently, in the mineral-resolved experiments of this study, namely

327   VOL, MG, and BM, dust mineralogy and dust size are the two factors affecting the SSA spatial

328   variation.

329   Conversely, in homogeneous dust experiments, specifically HD27 and HD09, SSA variation is

330   solely attributed to variation in dust size, as dust mineralogy remains uniform globally.

331   Interestingly, HD09 demonstrates smaller spatial variation (i.e., lower σ) in SSA compared to

332   HD27 (Figure 3a). To investigate the impact of dust size on SSA for different hematite content

333   (e.g., HD27 and HD09), we perform a simple test in Section S3 of the Supplement. Supplementary

334   Figure S3 illustrates that the variation of SSA due to the dust particle size is more pronounced with

335   increasing absorption, i.e., from HD09 to HD27. This suggests that enhancement in dust scattering

336   relative to dust absorption (i.e., an increase in SSA) mitigates the sensitivity of SSA to dust size.

337   The conclusions above provide an understanding of the SSA spatial variation (indicated by σ)

338   before (i.e., HD27 and HD09) and after (i.e., VOL, MG, and BM) implementing dust mineralogy.

339   The same σ (0.06) between HD27 and BM can be explained as follows: Because mineral-resolved

340   BM-mixing dust is overall more scattering than HD27 dust, resulting in a reduced sensitivity of

341   SSA to size, therefore, the σ of SSA caused by dust size is reduced in BM relative to HD27.

342   However, the incorporation of dust mineralogy in BM leads to an increase of σ. These contrasting

343   effects compensate for each other, resulting in the same σ. In contrast, HD09 is overall as

344   scattering as BM, as shown in Table 3 and Figure 3a, suggesting a similar sensitivity of SSA to

345   size. Therefore, the higher σ in BM relative to HD09 is attributed to the incorporation of dust

346   mineralogy. Worth to mention, AERONET dust is quite scattering as shown in Figure 3a, therefore

347   its SSA is less sensitive to dust size. The high σ (0.010) of AERONET SSA is mainly due to spatial

348   variations in dust mineral composition. Overall, reducing dust hematite content (HD09) leads to a

349   better agreement in mean SSA with AERONET (i.e., more scattering dust) but results in very low

350   σ (0.004), while implementing dust mineralogy (e.g., MG and BM) retains the agreement with

351   AERONET in mean SSA and, at the same time, increases σ (0.006).

352   Besides the standard deviation (σ), the slopes (k) obtained from the statistics of modeled SSA

353   versus AERONET SSA can also indicate the regional contrast of SSA. The regional contrast of

354   AERONET SSA is well captured by the model when k is one, underestimated when k is lower than

355   one, and overestimated when k is higher than one. As such, the slopes in Figure 3a show that the

356   contrast in SSA from different regions (e.g., North Africa vs. East Asia) observed by AERONET

357   is better captured by mineral-resolved experiments (k ranging from 0.22 to 0.27) than

358   homogeneous dust experiments (k ranging from 0.07 to 0.11). However, the modeled regional

359   contrast of SSA in mineral-resolved experiments remains overly underestimated (i.e., k is much

360   lower than one). The underestimation of regional SSA contrast in AM4.0 suggests the need for a

361   higher regional contrast in iron oxides content.
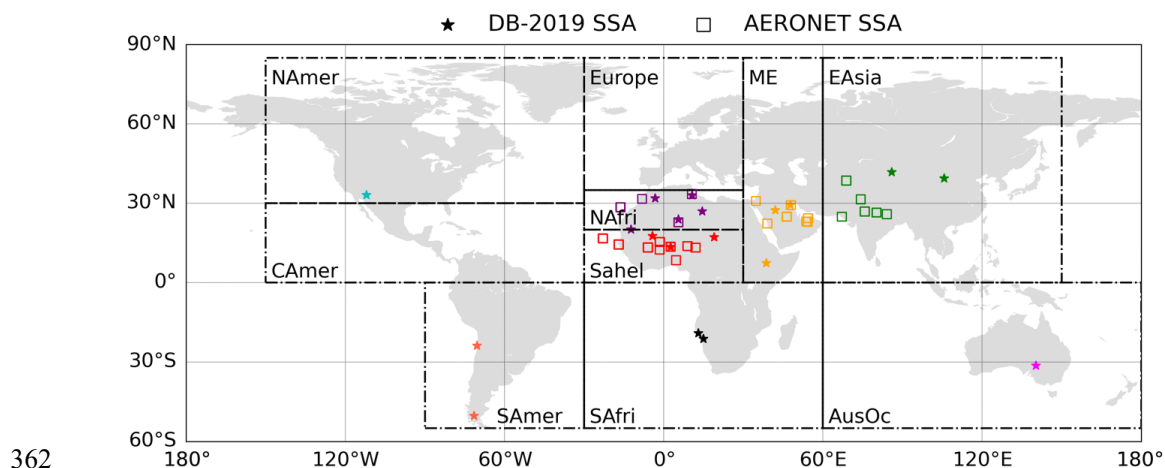
Figure 2. Dust sample locations in Di Biagio et al. (2019) and AERONET stations selected by filtering dust events. AERONET stations for SSA retrievals are in North Africa (NAfri), Sahel, the Middle East (ME) and East Asia (EAsia). Lab measurements by Di Biagio et al. (2017, 2019) expand dust sampling to include soils from North America (NAmer), South America (SAmer), South Africa (SAfri), Australia (AusOc).
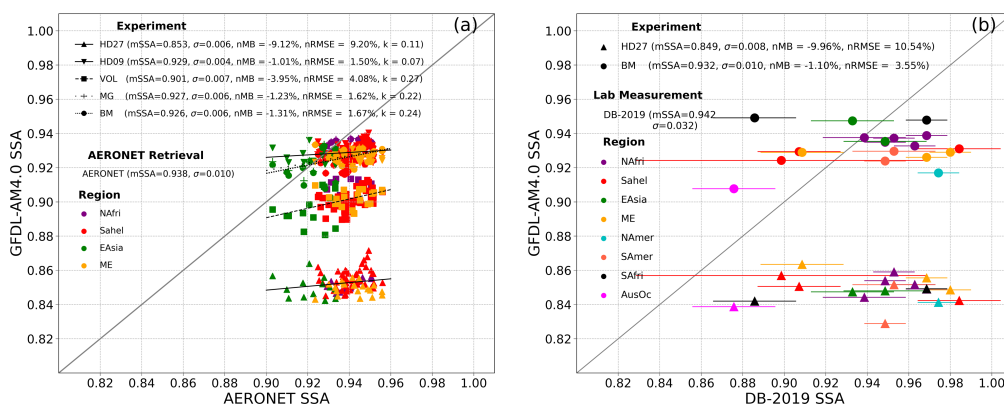
Figure 3. GFDL AM4.0 modeled 19-year (2001-2019) averaged monthly dust SSA (average in 0.44-0.625 µm) versus (a) AERONET 21-year (2000-2020) averaged monthly SSA retrievals (average at two visible wavelengths: 0.44 µm and 0.67 µm) and (b) laboratory SSA measurements (at 0.55 µm) of dust particles with diameter ranging from 0.2 μm up to $10 \mu m$ obtained by Di Biagio et al. (2019) (DB-2019). The lab measurements were carried out in March 2015, horizontal error bars represent measurement uncertainties. Markers represent different experiments, and colors represent different regions. mSSA in the legend represents the mean SSA averaged over all locations indicated in Figure 2 (squares for AERONET, stars for DB-2019). The standard deviation (σ), normalized mean bias (nMB), normalized root mean square error (nRMSE), and the slope of linear regression (k) are also indicated in the legend.

16

378 ### 4.2.2   Comparison with laboratory measurements

379   We further compare the GFDL AM4.0 modeled dust SSA (average in 0.44-0.625 μm) with DB-

380   2019 laboratory measurements of SSA at 0.55μm (Figure 3b). Figure 2 shows the locations where

381   dust samples were collected for the lab measurements. Considering that MG and BM are very

382   similar in terms of dust absorption and agree the best with AERONET SSA, we select BM as a

383   representative to compare with DB-2019 SSA. Moreover, to evaluate how dust absorption is

384   represented in the standard AM4.0 relative to lab measurements, we also show the comparison of

385   SSA between HD27 used in the standard AM4.0 and DB-2019 (Figure 3b). Consistent with the

386   comparison with AERONET, the comparison with lab measurements suggests that dust

387   representation in the standard AM4.0 (i.e., HD27) is excessively absorptive. The smaller nMB and

388   nRMSE values in BM suggests that SSA of BM agrees better with lab measurements.

389   Moreover, regarding spatial variation (σ), resolving dust mineralogy in BM increases σ from 0.008

390   for HD27 to 0.010 for BM, even though it is still lower than the σ (0.032) in DB-2019 lab

391   measurements. Note that the variation for HD27 results from the high sensitivity of SSA to dust

392   size due to its higher absorption (as discussed in Supplementary Section S3). The inability to

393   reproduce spatial variation observed in the lab measurements is likely attributed to two aspects.

394   The first limitation is the fact that samples of DB-2019 are from soils rather than aeolian dust.

395   Aeolian dust is expected to exhibit greater uniformity in mineralogy than soils because of the

396   atmospheric mixing of dust emitted from various soil sources. The second one is associated with

397   the under-representation of regional contrast in iron oxides content in our model. Observations

398   from the EMIT are therefore essential to constrain soil mineralogy in climate models.

399 ## 5   Impacts of dust mineralogy on climate

400   Resolving dust mineralogy in climate models affects dust optical properties (as discussed in

401   Section 4) and their spatial and temporal variability, thereby affecting their interactions with

402   shortwave (SW) and longwave (LW) radiation. The variability in dust radiative interactions further

403   induces the fast response of land surface temperature, circulation, and precipitation, which are

404   investigated in this section. To understand the impacts of dust minerals on climate, we proceed in

405   two steps. Firstly, we investigate the impacts of resolving dust mineralogy on radiation and climate

406   relative to the HD27 control run. The HD27 control run represents the standard GFDL AM4.0

407   model in which dust mineralogy is assumed to be temporally and spatially uniform, with a volume

408   fraction of 2.7% hematite. This step explores the influence of resolving dust mineralogy on climate

409   in the standard AM4.0 model. Secondly, we go beyond the representation of dust aerosols in the

410   standard AM4.0 model by replacing our homogeneous dust in HD27 control run with more

411   scattering homogeneous dust (i.e., HD09) to assess the impacts of resolving spatial and temporal

412   variations of dust mineralogy on climate relative to the HD09 experiment. As shown in Table 3

413   and Figure 3a, HD09 is much more scattering than HD27 and approximately as scattering as the

414   mineral-resolved dust (i.e., MG-mixing, and BM-mixing dust) in terms of globally averaged SSA.

415   Therefore, this step sheds light on the impacts of resolving dust mineralogy on climate given

416   similar globally averaged scattering properties with and without resolved dust mineralogy.

5.1   Impacts on Clear-sky Radiative Fluxes

418   We start our analysis by examining the impacts of resolving dust mineralogy on clear-sky radiative

419   fluxes. By 'clear-sky', we mean that our results do not consider the radiative effects of clouds.

420   Section S4 in the Supplement provides the clear-sky radiative fluxes anomalies at TOA and surface

421   (SFC) induced by resolving dust mineralogy over the global scale, we see much more significant

422   anomalies over the North Africa than other regions. Therefore, our study focuses on the North

423   Africa region, where the Sahara Desert, the largest dust source in the world, is located. The Sahara

424   (20°N-30°N, 10°W-35°E) and the Sahel (10°N-20°N, 10°W-35°E) regions are studied separately.

425   We specifically analyze the results for the June-July-August (JJA) season when dust loading is at

426   its highest and the West African Monsoon is the strongest.

427   The first column in Figure 4 illustrates the modeled clear-sky shortwave (SW), longwave (LW)

428   and net (NET: the combination of SW and LW) radiative flux at TOA from the HD27 control run.

429   Relative to HD27, mineral-resolved dust (i.e., VOL-mixing, MG-mixing, and BM-mixing dust)

430   generally reflects more SW radiation back to space and induces negative SW flux anomalies at

431   TOA (Figure 4 a-d; Positive: downward). In addition, MG-mixing and BM-mixing dust induce

432   stronger reflection anomalies than VOL-mixing dust. The results are consistent with the fact that

433   mineral-resolved dust is less absorptive than HD27 dust in the visible spectrum, and MG-mixing

434   and BM-mixing dust are even less absorptive than VOL-mixing dust, as discussed in Section 4.

435   Relative to the HD27 control run, the LW flux anomaly at TOA resulting from resolving

436   mineralogy is less substantial compared to SW flux anomaly (Figure 4 e-h). After combining both

437   SW and LW, resolving mineralogy turns out to induce substantial decrease in NET flux at TOA,

438   with a more than 50% negative anomaly over the Sahara and around a 20% negative anomaly over

439   the Sahel (see values in parentheses in Figure 4 i-l). Therefore, less NET radiation reaches the

440   Earth at TOA in the mineral-resolved dust cases due to their lower absorptivity.

441   At the surface (SFC) in Figure 5, the enhanced scattering of mineral-resolved dust scatters more

442   SW radiation toward Earth's surface, leading to a positive SW flux anomaly at SFC (Positive:

443   downward). In the LW, the cooling of the mineral-resolved dust layer, due to its low absorption,

444   results in less LW radiation emitted toward Earth's surface, causing a negative LW flux anomaly

445   at SFC. The positive anomalies in SW radiation are approximately canceled out by the negative

446   anomalies in LW radiation (Figure 5). As a result, a similar amount of radiation reaches the Earth's

447   surface in both HD27 and mineral-resolved cases. Despite less NET radiation entering the Earth

448   at TOA in mineral-resolved cases, the similar amount of NET radiation reaching the Earth's

449   surface indicates that less NET radiation is absorbed in the atmosphere in mineral-resolved cases.

450   As shown in Figure 6, the negative SW flux anomalies are partially offset by positive LW flux

451   anomalies, resulting in negative NET flux anomalies in the atmosphere. These anomalies amount

452   to approximately a 25% reduction over the Sahara and 10% reduction over the Sahel (see values

453   in parentheses in Figure 6 i-l).

454   Figure 7 shows the clear-sky fluxes anomalies with respect to HD09 over North Africa, the

455   anomalies over the global scale are shown in Figure S5, S7, and S9 in the Supplement. In contrast

456   to the anomalies with respect to HD27 control run, resolving dust mineralogy does not cause

457   substantial anomalies (< 5%) in clear-sky fluxes with respect to HD09 control run. This can be

458   attributed to their similarity in dust scattering properties, particularly SSA as shown in Figure 3.

459   The comparable effects of HD09 and mineral-resolved dust on radiation suggest that resolving

460   dust mineralogy does not have significant regionally averaged impacts on clear-sky fluxes when

461   homogeneous dust is as scattering as mineral-resolved dust aerosols. The equivalence between

462   HD09 and mineral-resolved dust in terms of their interactions with radiation may be related to the

463   three limitations in the current model simulations: 1) Soil mineralogy: The limited soil mineralogy

464   database fails to adequately capture the regional variation of iron content (or SSA) within the

465   region; 2) Dust emission based on Ginoux et al. (2001) uses a continuous function of topography,

466   which does not take into account geomorphological characteristics of the surface to differentiate

467   soil properties of dust sources as done by others (Zender et al., 2003; Bullard et al., 2011); 3) Dust

468   transport: Excessive numerical diffusion may occur when solving advection equation (Ginoux,

469   2003). Given all those limitations of our model simulations, this finding may differ with improved

470   representation of dust sources and transport. Such improvement may come from spaceborne soil

471   mineralogy dataset (e.g., EMIT) that may capture accurately the regional contrasts in iron oxides

472   content.

473   Furthermore, we conduct a comparison of modeled SW upward, LW upward, NET downward flux

474   at TOA with observation-based results from CERES_EBAF_Ed4.2 product (see Figure 8). The

475   difference between modeled flux and CERES observations are listed in parentheses within the title

476   of each figure in Figure 8. Compared to HD27, the more scattering HD09 and mineral-resolved

477   BM achieve much better agreement with CERES observations in clear-sky flux (i.e., SWup, LWup

478   and NETdn) at TOA. This is evident in the smaller values of HD09 – CERES (e.g., NETdn: 1.6

479   for the Sahara and 2.4 for the Sahel) and BM – CERES (e.g., NETdn: 0.4 for the Sahara and 2.1

480   for the Sahel) compared to HD07 – CERES (e.g., NETdn: 11.3 for the Sahara and 12.4 for the

481   Sahel), as shown by the values in parentheses in Figure 8. Between HD09 and BM, BM tends to

482   agree slightly better with CERES.
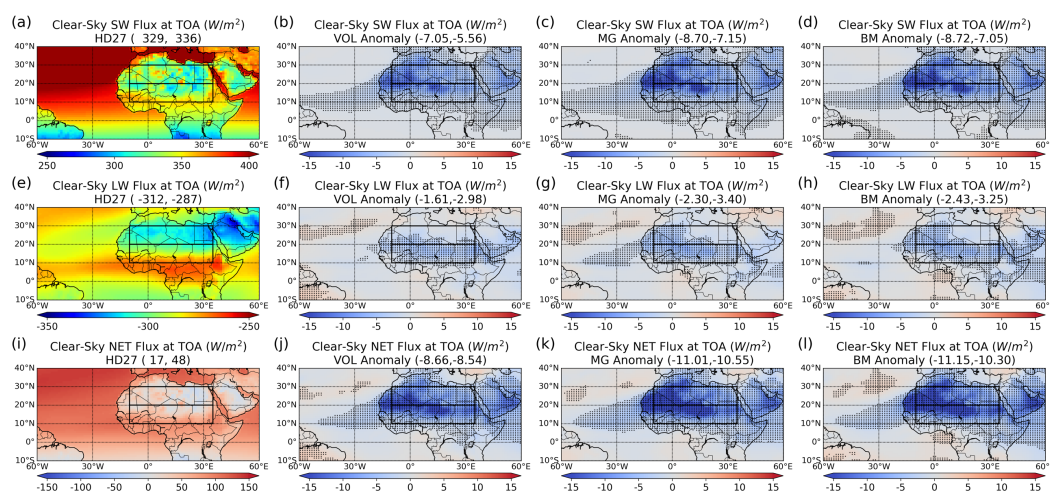
483

484   Figure 4. Seasonal mean JJA climatology (2001-2019) clear-sky SW (1st row), LW (2nd row) and

485   Net (3rd row) radiative flux at TOA for the HD27 control run (1st column) and their anomalies

486   resulting from resolving dust mineralogy in vol-mixing experiments (2nd column), Maxwell

487   Garnett mixing experiments (3rd column) and Bruggeman-mixing experiments (4th column).
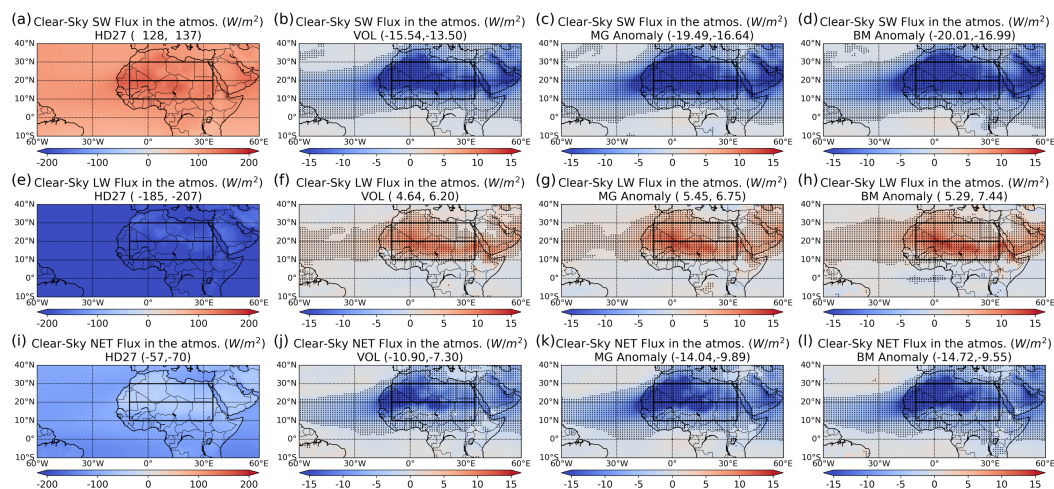
488   Downward direction is defined as positive. The dotted area denotes anomalies that are statistically

489   significant. The two values in parentheses within the title of each figure are domain average for

490   the Sahara and Sahel regions.
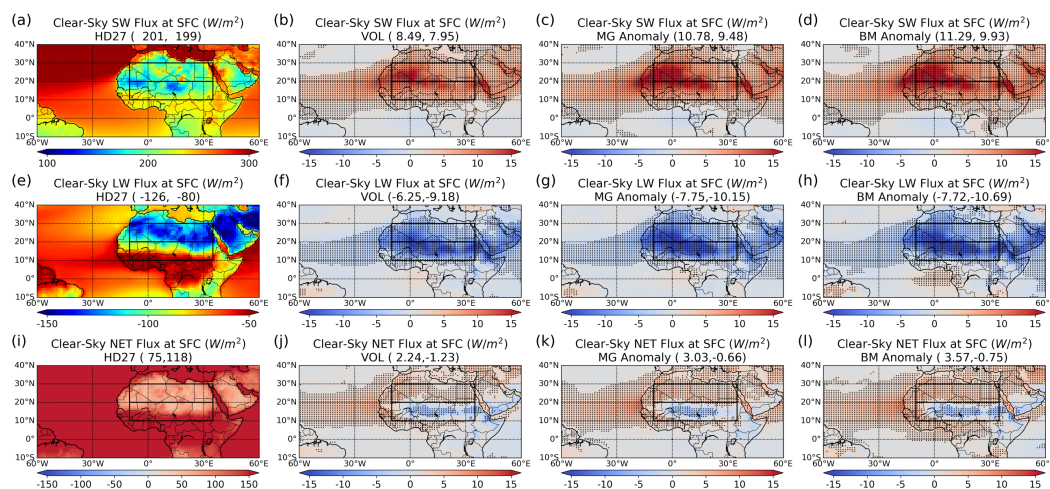
491
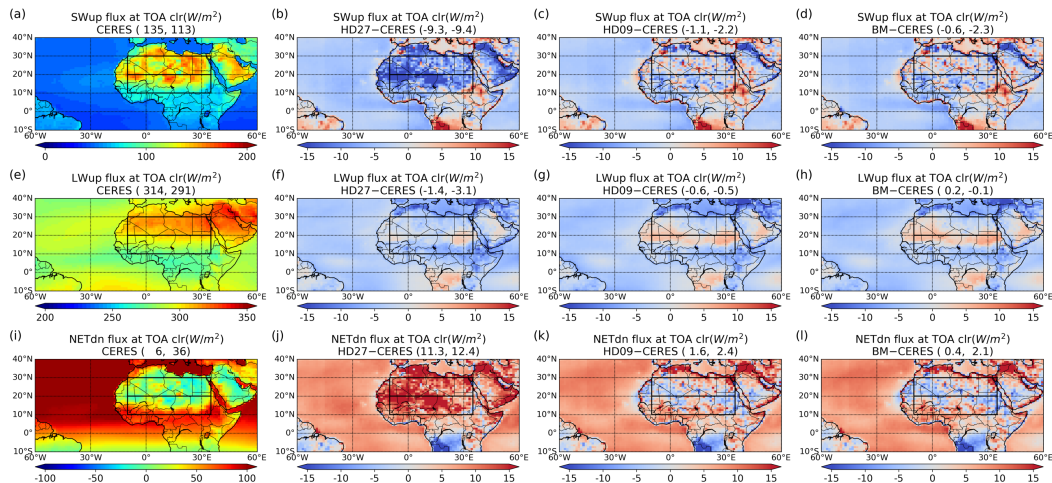
492   Figure 5. As in Figure 4, but for the surface.

493

494   Figure 6. As in the Figure 4, but for the radiative flux absorbed in the atmosphere.
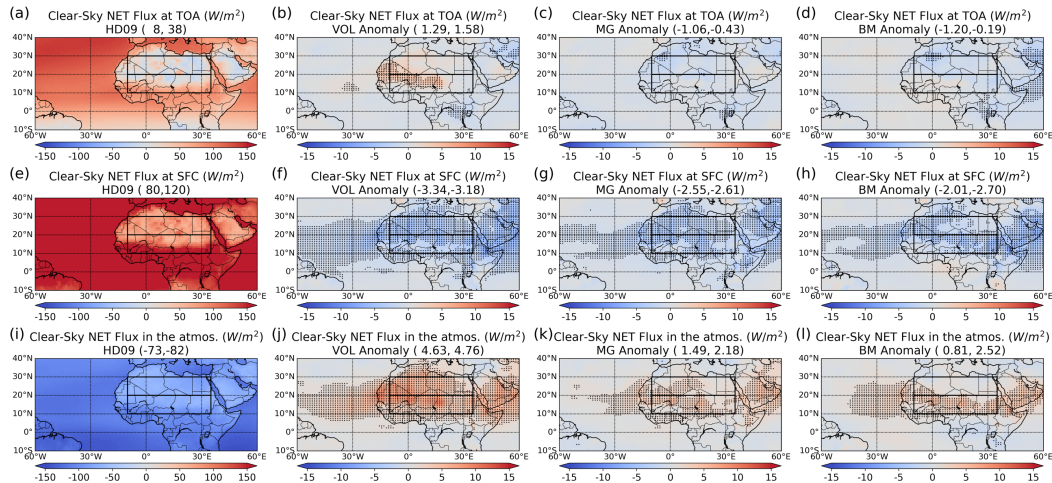
Figure 7. As in the Figure 4, but for HD09 control run. In addition, SW and LW flux anomalies are not shown here. Clear-sky net flux at TOA (1st row), at surface (2nd row), and in the atmosphere (3rd row) are shown in this figure.

Figure 8. Comparison of modeled clear-sky SW upward (SWup, 1st row), LW upward (LWup, 2nd row) and NET downward (NETdn, 3rd row) fluxes at TOA with CERES observation-based results over 2001-2019 JJA. The 1st column shows the clear-sky flux estimates at TOA from CERES_EBAF_Ed4.2 product, which represents clear-sky flux with clouds removed from the atmospheric column. The following columns show the difference of modeled clear-sky flux at TOA in HD27 (2nd column), HD09 (3rd column) and BM (4th column) experiments from CERES observations. The two values in parentheses within the title of each figure are domain average for the Sahara and Sahel regions. Specifically, the first column (CERES) is domain averaged flux, while the second (HD27 – CERES), third (HD09 – CERES), and fourth (BM – CERES) columns are domain averaged flux differences between model and CERES observation-based results.

510

5.2 Impacts on land temperature

512 Here we explore the impacts on the temperature vertical profile and near-land surface temperature.

513 Compared to the HD27 control run, lower absorption of radiation in the atmosphere by mineral-

514 resolved dust aerosols results in statistically significant negative temperature anomalies in the

515 atmosphere ranging from 800 mb up to 500 mb where dust aerosols are mainly located (Figure 9).

516 In contrast, there is no statistically significant temperature anomaly for mineral-resolved dust cases

517 compared to HD09 case. This result is consistent with the insignificant anomalies in clear-sky

518 radiative fluxes discussed in Section 5.1. In the subsequent part of the section, we compare our

519 mineral-resolved experiments (here we take BM as an example) with the HD27 control run to

520 further understand how dust aerosols with different optical properties affect land temperature.

521 Figure 10a shows air temperature at 2-meter from HD27 control run over the Northern Africa.

522 Near the land surface, more scattering mineral-resolved dust induces a temperature decrease (i.e.,

523 negative temperature anomaly -0.66 K) over the Sahara and a temperature increase (i.e., positive

524 temperature anomaly 0.70 K) over the Sahel as shown Figure 10b. To understand this phenomenon,

525 we further analyze the surface energy budget in Figure 10c-f.

526 Land equilibrates energy rather quickly with surface fluxes, namely the radiative flux, sensible

527 heat flux, latent heat flux and ground flux (i.e., downward heat flux into the ground). Precisely,

528 the radiative flux anomaly comprises two contributions: one is the instantaneous radiative forcing

529 (IRF) caused by the change in dust mineralogy in the atmosphere, and the other one is the

530 associated radiative feedbacks. For simplicity, we will not partition the radiative flux anomaly in

531 our discussion here. So, the radiative flux anomalies at land surface are quickly equilibrated by the

532 turbulent flux of energy through sensible heat flux, latent heat flux as well as ground flux, which

533 results in nearly zero net energy flux at land surface as shown in Figure 10f. Over the Sahel region,

534 the positive net radiative flux anomaly at land surface is balanced out by the increased sensible

535 heat flux and the decreased latent heat flux as well as ground flux. Note that the ground flux is

536 generally small in magnitude and not shown in Figure 10, but we include it in calculating net

537 surface energy flux in Figure 10f. The decrease of latent heat flux over the Sahel in BM case

538 (Figure 10d) is due to the depletion of soil moisture (and therefore evaporation) in the region as

539 shown in Figure 11. The depletion of soil moisture is caused by the decrease in moisture carried

540   by onshore winds over the Sahel and the decrease in precipitation over the same region, as will be

541   discussed in section 5.3. Therefore, a large enhancement of sensible heat flux ($\sim 5\ W/m^2$) is

542   needed (Figure 10c) not only to compensate for the depletion in latent heat flux ($\sim 3\ W/m^2$ in

543   Figure 10d), but also to balance out the increased net radiative flux ($\sim 2\ W/m^2$ in Figure 10e). As

544   a result, higher land surface temperature with anomaly around 0.6K is needed in the region to

545   achieve the required sensible heat flux enhancement.

546   Over the Sahara region, latent heat flux does not change from HD27 case to BM case, therefore,

547   the increased net radiative flux ($\sim 3.3\ W/m^2$) in BM compared to HD27 is mainly balanced out by

548   the enhanced sensible heat flux ($\sim 3.4\ W/m^2$) which requires a larger temperature gradient

549   between surface and atmosphere. However, there is a very strong negative temperature anomaly

550   (around −1K) in the atmosphere near 700 hPa due to less dust absorption in BM as we discussed

551   in Figure 9. The strong negative temperature anomaly in the lower atmosphere effectively

552   increases the vertical temperature gradient. As such, it is not necessary for the land surface

553   temperature to increase; in fact, it may need to decrease by approximately 0.39 K to achieve the

554   desired enhancement in sensible heat flux and reach equilibrium.

555   Additionally, to assess the effectiveness of various dust scattering properties (e.g., HD27, HD09,

556   and BM) in matching observations of near-surface temperature, we compare the modeled near

557   surface temperature (T_{2m}) with CRU TS observations, which is described in Section 2.6, over the

558   Sahara and Sahel regions (Table 4). Considering the relatively large inter-model spread of regional

559   surface air temperature, we compare the Sahara-Sahel regional contrast in surface air temperature

560   to the CRU rather than comparing their absolute values. Table 4 shows that HD09 and BM improve

561   the agreement with CRU in Sahara-Sahel temperature contrast compared to HD27, and BM

562   exhibits the closest agreement with CRU.
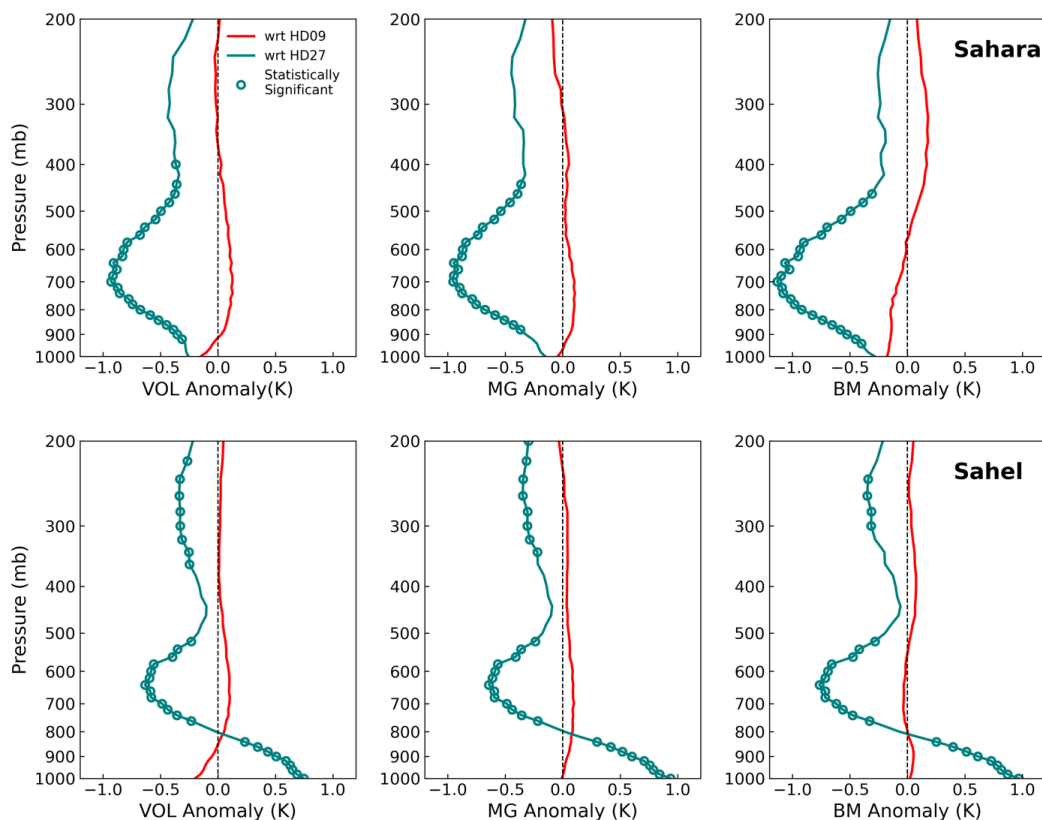
24

Figure 9. Vertical profile of temperature anomaly induced by resolving dust mineralogy for the Sahara (1st row) and the Sahel (2nd row) regions in the three mineral-resolved experiments (i.e., VOL, MG, BM). Green lines represent temperature anomalies with respect to HD27 control run. Red lines are temperature anomalies with respect to HD09 control run. The circles represent statistically significant temperature anomaly.
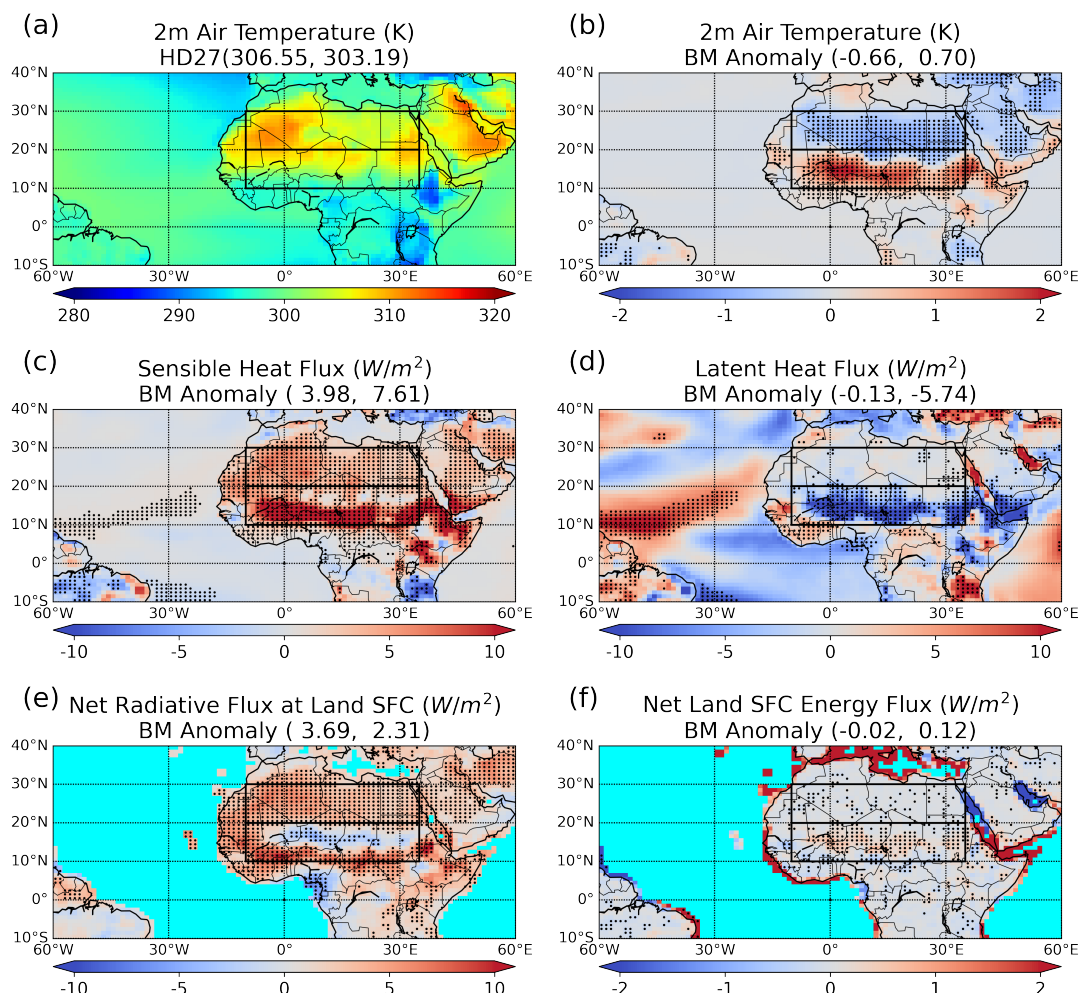
Figure 10. Air temperature at 2-meter from HD27 control run (a), anomaly (b) induced by implementing Bruggeman-mixing minerals in BM experiment, surface sensible heat flux (c), latent heat flux (d), net radiative flux (e), net energy flux (f) anomalies between BM and HD27; Upward flux is positive in (c) and (d), while downward flux is positive in (e) and (f). Net energy flux (f) is the subtraction of (c), (d), and downward ground flux from (e). Note that ground flux is not shown in the figure considering its relatively small magnitude, but it is included in the land surface net energy flux calculations in subplot (f). The dotted area denotes anomalies that are statistically significant. The two values in parentheses within the title of each figure are domain average for the Sahara and Sahel regions.

579

580
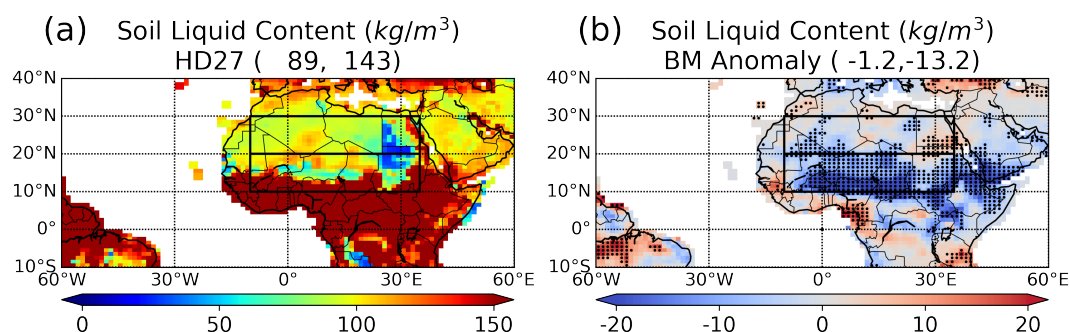
Figure 11. Soil liquid content in HD27 control run (a) and anomaly resulting from implementing
Bruggeman-mixing minerals in the BM experiment (b). The two values in parentheses within the title of
each figure are domain average for the Sahara and Sahel regions.

Table 4. The 19-year (2001~2019) JJA mean 2-meter Air Temperature (T_{2m}, unit: K) and their standard
deviation from CRU observations and modeled experiments over the Sahara and Sahel regions. The
'Contrast' row indicates the T_{2m} regional contrast between the Sahara and the Sahel.

Region	CRU (K)	HD27 (K)	HD09 (K)	BM (K)
Sahara	305.8 ± 0.18	306.55 ± 0.52	306.2 ± 0.68	305.89 ± 0.61
Sahel	304.1 ± 0.32	303.19 ± 0.46	303.87 ± 0.51	303.89 ± 0.59
Contrast	1.7 ± 0.5	3.36 ± 0.98	2.3 ± 1.19	2.0 ± 1.2

587

5.3 Impacts on winds and precipitation

To understand the fast circulation and hydrological response resulting from resolving dust
mineralogy, we examine surface wind speed anomalies (Figure 12) and precipitation anomalies
(Figure 13) induced by mineral-resolved dust. Based on the elevated heat pump (EHP) mechanism
of Lau et al., (2009), more absorptive dust absorbs radiation and redistributes heating from the
surface to within the dust layer (Miller and Tegen, 1998; Strong et al., 2015). Atmospheric heating
leads to ascent thus enhancing precipitation. In this sense, more scattering mineral-resolved dust
aerosols absorb less radiation and cause less warming of the atmosphere, suppressing ascent
motion and reducing precipitation.

597 As discussed in the Section 4.1, mineral-resolved dust (i.e., VOL, MG, and BM) is more scattering

598 than HD27. Relative to HD27 case, mineral-resolved dust causes less warming of the atmosphere

599 due to less absorption and suppresses ascent. The suppressed ascent is associated with a reduction

600 both in the wind divergence aloft and in convergence at the surface. The reduction in convergence

601 results in northeast wind anomalies at 10-meter over the Sahel (Figure 12a, b), which are opposite

602 in direction to the southwest onshore winds of the West African Monsoon. The inhibition of

603 onshore winds, bringing less moisture to the Sahel, combined with the suppression of ascent

604 motion work together to reduces precipitation over this region (Figure 13a, b).

605 Besides the Sahel, there is a statistically significant positive anomaly (0.28 mm/day) of

606 precipitation over the region to the south of the Sahel in BM relative to HD27 (Figure 13b), we

607 will call this region as the Guinea Coast (GC: 0-10°N, 10°W-15°E) region. One possible reason

608 for the increase of precipitation over the GC is that the region is located to the south of the Saharan

609 dust layer, the suppression of ascent over the Sahel in BM suppresses the subsidence in the GC

610 region, therefore, enhances the precipitation.

611 These changes in precipitation pattern have non-negligible effects on soil moisture content in

612 North Africa due to its moisture-starved environment. The decrease in precipitation over the Sahel

613 in BM leads to a reduction in soil moisture content. Conversely, the increase of precipitation over

614 the GC leads to increases of soil moisture content (Figure 11). The change in soil moisture content

615 further affects the partitioning of surface energy fluxes and the efficiency of the latent heat flux,

616 thereby affecting land surface temperature, as illustrated by Figure 10.

617 So far, we have been focusing on discussing the impacts of resolving dust mineralogy on winds

618 and precipitation relative to HD27 control run. The large discrepancy in optical properties between

619 HD27 and mineral-resolved dust allows us to better understand how dust aerosols with varying

620 optical properties impact our climate through their distinct radiative effects. As discussed in

621 section 4.1, HD09 dust is nearly as scattering as mineral-resolved dust but exhibits smaller regional

622 variability. Section 5.1 shows that resolving dust mineralogy does not lead to statistically

623 significant anomalies on radiation relative to HD09. Consistently, there are no further statistically

624 significant impacts on winds (Figure 12c, d) and precipitation (Figure 13c, d).

625 Furthermore, to investigate the effectiveness of various dust scattering properties (e.g., HD27,

626 HD09, BM) in matching observations of precipitation rate, we compare the modeled precipitation

627   with CRU TS observations over the Sahara, Sahel and GC regions (Table 5). The greater difference

628   between HD09, BM and CRU (i.e., HD09 − CRU and BM − CRU) indicate that more scattering

629   HD09 and BM lead to larger discrepancy between the modeled precipitation and CRU

630   observations. This discrepancy may reflect non-dust biases in model precipitation, or the absence

631   of the slow climate response, whose inclusion can change even the sign of the precipitation

632   anomaly within the WAM (Miller and Tegen, 1998; Jordan et al., 2018).
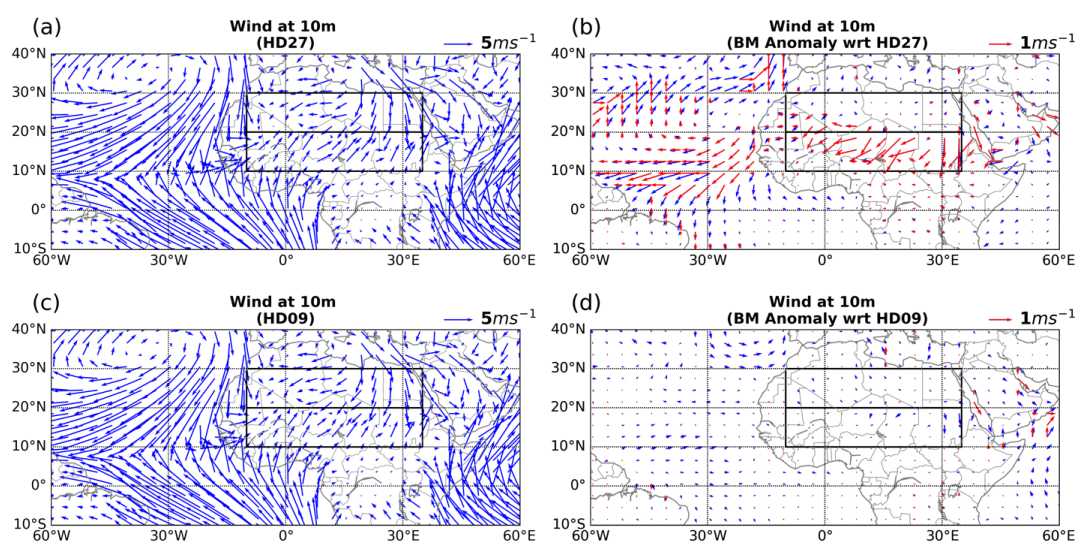
633

634   Figure 12. Surface wind at 10-meter from HD27 (a) and HD09 (c) control runs and their anomalies (b) and
635   (d) resulting from implementing Bruggeman-mixing minerals in the BM experiment. Statistically
636   significant wind anomalies are highlighted by red arrows.
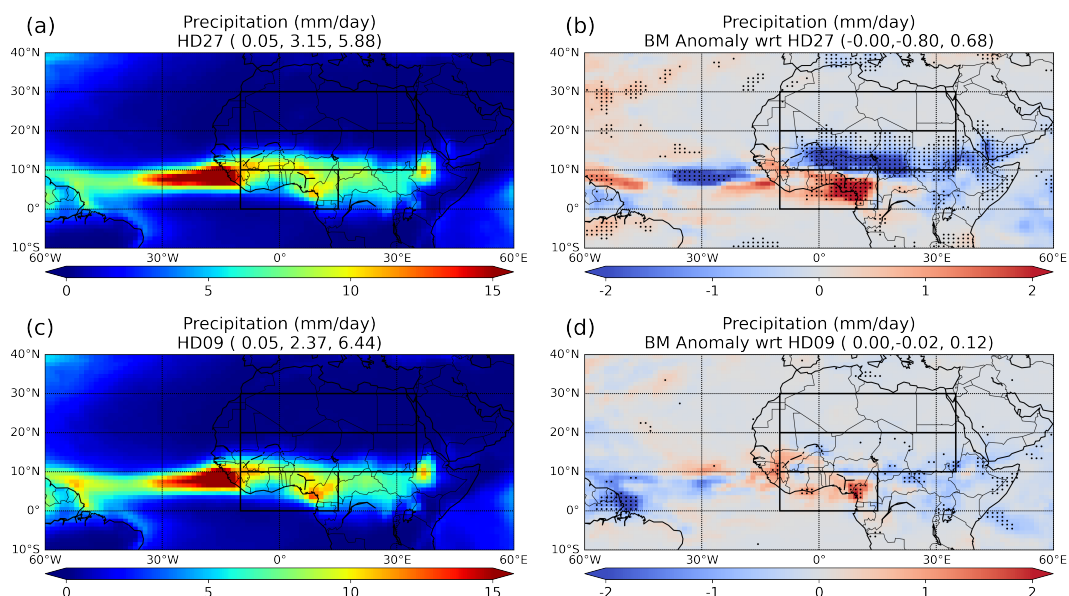
Figure 13. 19-year (2001-2019) JJA mean precipitation from HD27 (a) and HD09 (c) control runs and anomalies resulting from implementing Bruggeman-mixing minerals with respect to HD27 (b) and with respect to HD09 (d). The three values in the parenthesis are domain averaged values for the Sahara, Sahel, and GC regions. Note, for anomalies, we only average the dotted area, in other words, we only calculate the domain average of statistically significant anomalies.

Table 5. Comparison of modeled precipitation rate (PRE, unit: mm/day) with observations from CRU TS dataset over 2001-2019 JJA. CRU column represents 19-year (2001-2019) JJA mean PRE over the region as well as 19-year standard deviation (std). HD27 − CRU column shows the 19-year mean PRE difference between HD27 control run and CRU observations, along with the corresponding std of this 19-year difference. Similar for HD09 − CRU and BM − CRU.

Comparison / Region	CRU (mm/day)	HD27 − CRU (mm/day)	HD09 − CRU (mm/day)	BM − CRU (mm/day)
Sahara	0.08 ± 0.013	-0.03 ± 0.03	-0.03 ± 0.07	-0.04 ± 0.05
Sahel	2.99 ± 0.27	0.16 ± 0.56	-0.62 ± 0.43	-0.71 ± 0.41
Guinea Coast	6.16 ± 0.49	-0.28 ± 0.90	0.28 ± 1.02	0.64 ± 0.83

6   Potential for reducing mineral tracers

Thus far in this study, we have been using 45 mineral tracers in mineral-resolved experiments (i.e., VOL, MG, and BM). However, it is important to investigate the potential of reducing the number of mineral tracers in climate models to lower computational costs. In this section, we take BM as a reference for providing the best comparisons with CRU temperature and CERES flux observations, and conduct an experiment named BM-RT to assess the possibility of reducing mineral tracers in BM. The BM-RT experiment consists of three sub-experiments, namely, BM-LC, BM-LCRH, and BM-LCRHRG. In each of the three sub-experiments, the number of mineral tracers is progressively reduced, allowing for an examination of the relative impacts of different minerals on climate compared to the reference BM.

As discussed in section 4.1, the three clay minerals (i.e., illite, kaolinite, smectite) exhibit similar optical properties and perform similar functions in climate by hosting hematite. Hence, they can be combined in their interaction with radiation without significant impacts on climate. In addition, by lumping the three clay minerals together, the number of mineral tracers can be reduced from 45 in BM (nine types of minerals × five size bins) to 35 (seven types of minerals × five size bins). Therefore, in the first sub-experiment BM-LC (where 'LC' represents 'Lump Clay minerals'), we lump together the three clay minerals as one mineral species 'clay433'.

Externally mixed hematite is mainly concentrated over the Sahel region (Ginoux et al. 2023, in preparation) and cannot be transported to remote regions due to its high density. Obiso et al. (2023) shows that extinction due to external hematite is negligible compared to internally mixed hematite and other minerals. Thus, we further remove external hematite tracers in the second sub-experiment BM-LCRH (where 'RH' indicates 'Remove externally mixed Hematite'). The mass fraction of external hematite is combined with internal hematite to ensure that the total mineral fraction at emission remains equal to one. In this sub-experiment, the number of mineral tracers is reduced from 35 in BM-LC to 30 in BM-LCRH.

Since there are no known specific impacts of gypsum on climate, we conducted the third sub-experiment, BM-LCRHRG ('RG' indicates 'Remove Gypsum'), where gypsum was removed. The mass fraction previously attributed to gypsum at emission, which is very low at the global scale, was proportionally redistributed among all other minerals. The number of mineral tracers is finally reduced from 30 in BM-LCRH to 25 in BM-LCRHRG.

679   We analyze the 19-year (2001-2019) time series of total dust mineral emission before and after

680   reducing mineral tracers in Figure 14. We observe subtle differences in total mineral emission

681   between experiments, which arises from the feedback of mineral radiative interactions. However,

682   these differences are numerically small, and Student's t-test suggests that the time series of the

683   four experiments are not statistically different. Additionally, the globally averaged DAOD and

684   SSA of each sub-experiment remains highly similar to those of the reference experiment BM, as

685   listed in Table 3.
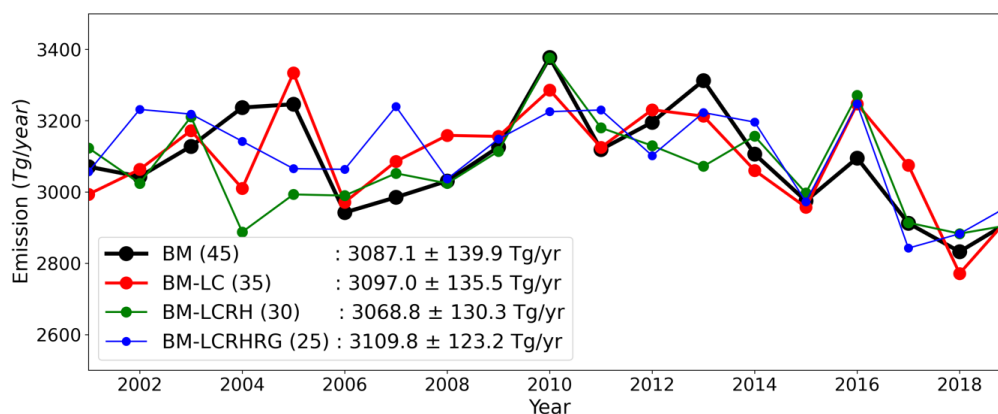
686

687 Figure 14. Time series of total dust mineral emission from 2001 to 2019 before and after reducing the
688 number of mineral tracers. The legend displays the following information: 'Experiment name (number of
689 mineral tracers): 19-year averaged total mineral emission ± 19-year standard deviation of total mineral
690 emission'.

691   Given the highly similar optical properties of minerals before and after reducing mineral tracers,

692   we further investigate their impact on climate. Firstly, we examine the clear-sky flux anomaly of

693   each of the three sub-experiments at TOA and surface relative to the reference experiment BM, as

694   shown in Supplementary Figure S12 for TOA and Supplementary Figure S13 for surface. We only

695   observe a few statistically significant (p-value < 0.05) anomalies over the North Africa, suggesting

696   that the reduction of mineral tracers in the three sub-experiments has a weak impact on radiation.

697   Furthermore, we investigate the anomaly in temperature profile, surface winds, and precipitation

698   of each of the three sub-experiments relative to the reference experiment BM. The results are

699   presented in Figure S14-S16 in the Supplement. No statistically significant (p-value < 0.05)

700   temperature anomalies (Figure S14) and surface wind anomalies (Figure S15) is observed. Only a

701   few statistically significant anomalies in precipitation are observed in the Supplementary Figure

702   S16. These results suggest that the reduction of mineral tracers in the three sub-experiments has a

703   weak impact on climate.

704   The results from the BM-RT experiment suggest combining clay minerals and excluding the

705   externally mixed hematite and gypsum in the dust mineral implementation. The removal of mineral

706   tracers reduces the number of mineral tracers from 45 to 25, effectively lowering computational

707   costs without causing statistically significant impacts on simulating climate.

7   Conclusions

709   We simulate the distribution of dust mineralogy (i.e., illite, kaolinite, smectite, hematite, calcite,

710   feldspar, quartz, and gypsum) in the GFDL AM4.0 model. Our investigation focuses on the

711   radiative impacts of resolving dust mineralogy on Earth's atmosphere and its fast response of land

712   temperature, surface winds and precipitation.

713   We set up two control runs: HD27 and HD09, in which dust mineralogy is considered as

714   temporally and spatially uniform, the former following the standard configuration for the dust

715   optical properties in GFDL AM4.0 and the latter including a more scattering dust. Three

716   experiments with resolved mineralogy are also conducted: VOL, MG, and BG, using three

717   different mixing rules for the internal mixture between hematite and clay minerals (i.e., volume

718   weighted mean, Maxwell Garnett, and Bruggeman). The comparison of dust absorption properties

719   (SSA) with observation-based results suggests that the homogeneous dust used in the standard

720   GFDL AM4.0 (i.e., HD27) is overly absorptive. Compared to HD27, the homogeneous dust with

721   reduced hematite content (HD09) and mineral-resolved dust (i.e., MG and BM) exhibit much

722   better agreement with AERONET retrievals and laboratory measurements in terms of dust

723   absorption properties (i.e., SSA). Additionally, mineral-resolved dust enhances regional variability

724   in dust SSA compared to homogenous dust, further improves the agreement with AERONET, even

725   though it remains lower than the observed variability.

726   The two homogeneous dust control runs, HD27 and HD09, with distinct dust absorption properties,

727   allow us to investigate the impact of dust mineralogy on Earth's radiation and fast climate response.

728   During JJA, compared to HD27, resolving dust mineralogy results in a reduction of over 50% in

729   NET downward radiation across the Sahara and approximately 20% over the Sahel at TOA.

730   Additionally, there is a reduction of around 25% in the atmospheric absorption of radiation over

731   the Shahara and around 10% over the Sahel in the atmosphere. The reduced surface absorption of

732   radiation by mineral-resolved dust leads to a temperature decrease of 0.39K at the land surface

733   across the Sahara and an increase of 0.6K over the Sahel. The reduced NET downward radiation

734   at TOA, attributed to the less absorption of radiation by mineral-resolved dust, suppresses ascent

735   and weakens the monsoon inflow from the Gulf of Guinea. This brings less moisture to the Sahel,

736   which combined with decreased ascent induces a reduction of precipitation. On the other hand,

737   resolving dust mineralogy does not lead to statistically significant changes in all above-mentioned

738   aspects compared to HD09. The models with reduced absorption (HD09 and fully resolved

739   mineralogy) improve the comparison with observations of CERES fluxes and CRU land surface

740   temperature. We see a slightly better agreement with observations for fully resolved mineralogy

741   than HD09 however it is not statistically significant. As such, when using fixed mineralogical

742   composition, we recommend using a 0.9% hematite content in volume, which represents the lowest

743   of the three hematite mixings considered by Balkanski et al. (2007). However, our

744   recommendation is directed toward the GFDL AM4.0 model with all its uncertainties related to

745   mineral distribution, emission sources, and aerosol transport. Moreover, incorporating dust

746   mineralogy in models is likely to be important also in other aspects, such as cloud properties, ocean

747   biogeochemistry, air quality and photochemistry. For studies with resolved mineralogy, we show

748   that the number of mineral tracers can be reduced from 45 to 25 without losing the quality of

749   comparison with observations of CERES fluxes and CRU surface temperature. Such reduction can

750   be achieved by lumping together clay minerals, removing external hematite and gypsum. For

751   specific research such as biogeochemistry, it may be necessary to fully resolve mineralogy to

752   achieve accuracy.

753   This study has some limitations. First, the soil mineralogy map from C1999 is based on extensive

754   extrapolation and limited observations. In terms of the need to improve knowledge of soil

755   mineralogy in dust source regions, the launch in July 2022 of the EMIT instrument operating from

756   the International Space Station will provide mineral identifications of dust sources using

757   hyperspectral measurements (Green et al., 2020). The EMIT soil map measurements will improve

758   resolving dust mineralogy in climate models and advance our understanding of dust's effects in

759   the Earth system. Second, hematite and goethite are the most common iron oxides present in soils.

760   However, goethite is not considered in this study because not included in the used soil mineralogy

761   map. Previous studies suggest that goethite is generally more abundant than hematite, but it is less

762   absorptive than hematite in the visible spectrum (Formenti et al., 2014). Therefore, the abundance

763   of iron oxides may be underestimated in this study, which may lead to underestimation of dust

764   absorption in the SW. A more recent database by Journet et al. (2014) (J2014) includes the

765   distribution of goethite but it shares many limitations as C1999 (e.g., extensive extrapolation) and

766   has other major disadvantages, such as numbers of missing soil fractions of some minerals at some

767   locations. Third, the refractive index of hematite used in our study is close to the upper range of

768   the values available in literature (Zhang et al., 2015). Hence, the last two limitations,

769   underestimation of iron oxide content and overestimation of absorption by hematite, may have

770   compensating effects.

771   This study, by prescribing SST, calculates only the fast response to the dust DRE. This complicates

772   model evaluation because the observations include the slow response to dust. Variables like

773   precipitation are especially sensitive to the inclusion of the slow response because prescribed SST

774   experiments omit the surface energy balance over the ocean. Thus, the surface DRE beneath the

775   aerosol layer, which is generally negative, is not fully balanced by a fast reduction of evaporation

776   (Miller et al., 2004).The addition of the surface balance in the slow response can reverse the sign

777   of the fast precipitation anomaly (Miller and Tegen, 1998; Jordan et al., 2018). In this study, the

778   increase of dust scattering (e.g., through consideration of dust mineral composition) generally

779   reduces model biases for all variables except precipitation.

8 Competing interests

The contact author has declared that none of the authors has any competing interests.

9 Acknowledgement

10 References

Atkinson, J. D., Murray, B. J., Woodhouse, M. T., Whale, T. F., Baustian, K. J., Carslaw, K. S., Dobbie, S., O'Sullivan, D., and Malkin, T. L.: The importance of feldspar for ice nucleation by mineral dust in mixed-phase clouds, Nature, 498, 355–358, https://doi.org/10.1038/nature12278, 2013.

Balkanski, Y., Schulz, M., Claquin, T., and Guibert, S.: Reevaluation of Mineral aerosol radiative forcings suggests a better agreement with satellite and AERONET data, Atmos. Chem. Phys., 7, 81–95, https://doi.org/DOI 10.5194/acp-7-81-2007, 2007.

Di Biagio, C., Formenti, P., Balkanski, Y., Caponi, L., Cazaunau, M., Pangui, E., Journet, E., Nowak, S., Caquineau, S., Andreae O, M., Kandler, K., Saeed, T., Piketh, S., Seibert, D., Williams, E., and Doussin, J. F. C.: Global scale variability of the mineral dust long-wave refractive index: A new dataset of in situ measurements for climate modeling and remote sensing, Atmos. Chem. Phys., 17, 1901–1929, https://doi.org/10.5194/acp-17-1901-2017, 2017.

Di Biagio, C., Formenti, P., Balkanski, Y., Caponi, L., Cazaunau, M., Pangui, E., Journet, E., Nowak, S., Andreae, M. O., Kandler, K., Saeed, T., Piketh, S., Seibert, D., Williams, E., and Doussin, J. F.: Complex refractive indices and single-scattering albedo of global dust aerosols in the shortwave spectrum and relationship to size and iron content, Atmos. Chem. Phys., 19, 15503–15531, https://doi.org/10.5194/acp-19-15503-2019, 2019.

Bian, H. and Zender, C. S.: Mineral dust and global tropospheric chemistry: Relative roles of photolysis and heterogeneous uptake, J. Geophys. Res. Atmos., 108, https://doi.org/10.1029/2002jd003143, 2003.

Bullard, J. E., Harrison, S. P., Baddock, M. C., Drake, N., Gill, T. E., McTainsh, G., and Sun, Y.: Preferential dust sources: A geomorphological classification designed for use in global dust-cycle models, J. Geophys. Res. Earth Surf., 116, https://doi.org/10.1029/2011JF002061, 2011.

Chatziparaschos, M., Daskalakis, N., Myriokefalitakis, S., Kalivitis, N., Nenes, A., Goncalves Ageitos, M., Costa-Suros, M., Perez Garcia-Pando, C., Zanoli, M., Vrekoussis, M., and Kanakidou, M.: Role of K-feldspar and quartz in global ice nucleation by mineral dust in mixed-phase clouds, Atmos. Chem. Phys., 23, 1785–1801, https://doi.org/10.5194/acp-23-1785-2023, 2023.

Claquin, T., SCHULZ, M., BALKANSKI, Y., and BOUCHER, O.: Uncertainties in assessing

828   radiative forcing by mineral dust, Tellus B, 50, 491–505, https://doi.org/10.1034/j.1600-
829   0889.1998.t01-2-00007.x, 1998.

830   Claquin, T., Schulz, M., and Balkanski, Y. J.: Modeling the mineralogy of atmospheric dust
831   sources, J. Geophys. Res. Atmos., 104, 22243–22256, https://doi.org/10.1029/1999JD900416,
832   1999.

833   Dentener, F. J., Carmichael, G. R., Zhang, Y., Lelieveld, J., and Crutzen, P. J.: Role of mineral
834   aerosol as a reactive surface in the global troposphere, J. Geophys. Res. Atmos., 101, 22869–22889,
835   https://doi.org/10.1029/96jd01818, 1996.

836   Dubovik, O., Holben, B., Eck, T. F., Smirnov, A., Kaufman, Y. J., King, M. D., Tanre, D., and
837   Slutsker, I.: Variability of absorption and optical properties of key aerosol types observed in
838   worldwide locations, J. Atmos. Sci., 59, 590–608, https://doi.org/Doi 10.1175/1520-
839   0469(2002)059<0590:Voaaop>2.0.Co;2, 2002.

840   Dunne, J. P., Horowitz, L. W., Adcroft, A. J., Ginoux, P., Held, I. M., John, J. G., Krasting, J. P.,
841   Malyshev, S., Naik, V., Paulot, F., Shevliakova, E., Stock, C. A., Zadeh, N., Balaji, V., Blanton,
842   C., Dunne, K. A., Dupuis, C., Durachta, J., Dussin, R., Gauthier, P. P. G., Griffies, S. M., Guo, H.,
843   Hallberg, R. W., Harrison, M., He, J., Hurlin, W., McHugh, C., Menzel, R., Milly, P. C. D.,
844   Nikonov, S., Paynter, D. J., Ploshay, J., Radhakrishnan, A., Rand, K., Reichl, B. G., Robinson, T.,
845   Schwarzkopf, D. M., Sentman, L. T., Underwood, S., Vahlenkamp, H., Winton, M., Wittenberg,
846   A. T., Wyman, B., Zeng, Y., and Zhao, M.: The GFDL Earth System Model Version 4.1 (GFDL-
847   ESM 4.1): Overall Coupled Model Description and Simulation Characteristics, J. Adv. Model.
848   Earth Syst., 12, https://doi.org/10.1029/2019MS002015, 2020.

849   Evans, S., Malyshev, S., Ginoux, P., and Shevliakova, E.: The Impacts of the Dust Radiative Effect
850   on Vegetation Growth in the Sahel, Global Biogeochem. Cycles, 33, 1582–1593,
851   https://doi.org/10.1029/2018GB006128, 2019.

852   Formenti, P., Caquineau, S., Chevaillier, S., Klaver, A., Desboeufs, K., Rajot, J. L., Belin, S., and
853   Briois, V.: Dominance of goethite over hematite in iron oxides of mineral dust from Western
854   Africa: Quantitative partitioning by X-ray absorption spectroscopy, J. Geophys. Res. Atmos., 119,
855   12,740-12,754, https://doi.org/10.1002/2014JD021668, 2014.

856   Gates, W. L.: AMIP: the Atmospheric Model Intercomparison Project, Bull. - Am. Meteorol. Soc.,

857   73, 1962–1970, https://doi.org/10.1175/1520-0477(1992)073<1962:ATAMIP>2.0.CO;2, 1992.

858   Giles, D. M., Sinyuk, A., Sorokin, M. G., Schafer, J. S., Smirnov, A., Slutsker, I., Eck, T. F.,

859   Holben, B. N., Lewis, J. R., Campbell, J. R., Welton, E. J., Korkin, S. V., and Lyapustin, A. I.:

860   Advancements in the Aerosol Robotic Network (AERONET) Version 3 database - Automated

861   near-real-time quality control algorithm with improved cloud screening for Sun photometer

862   aerosol optical depth (AOD) measurements, Atmos. Meas. Tech., 12, 169–209,

863   https://doi.org/10.5194/amt-12-169-2019, 2019.

864   Ginoux, P.: Effects of nonsphericity on mineral dust modeling, J. Geophys. Res. Atmos., 108,

865   https://doi.org/10.1029/2002jd002516, 2003.

866   Ginoux, P., Chin, M., Tegen, I., Prospero, J. M., Holben, B., Dubovik, O., and Lin, S. J.: Sources

867   and distributions of dust aerosols simulated with the GOCART model, J. Geophys. Res., 106,

868   20255–20273, https://doi.org/10.1029/2000jd000053, 2001.

869   Gliß, J., Mortier, A., Schulz, M., Andrews, E., Balkanski, Y., Bauer, S. E., Benedictow, A. M. K.,

870   Bian, H., Checa-Garcia, R., Chin, M., Ginoux, P., Griesfeller, J. J., Heckel, A., Kipling, Z.,

871   Kirkeväg, A., Kokkola, H., Laj, P., Le Sager, P., Tronstad Lund, M., Lund Myhre, C., Matsui, H.,

872   Myhre, G., Neubauer, D., Van Noije, T., North, P., Olivié, D. J. L., Rémy, S., Sogacheva, L.,

873   Takemura, T., Tsigaridis, K., and Tsyro, S. G.: AeroCom phase III multi-model evaluation of the

874   aerosol life cycle and optical properties using ground- And space-based remote sensing as well as

875   surface in situ observations, Atmos. Chem. Phys., 21, 87–128, https://doi.org/10.5194/acp-21-87-

876   2021, 2021.

877   Gonçalves Ageitos, M., Obiso, V., Miller, R. L., Jorba, O., Klose, M., Dawson, M., Balkanski, Y.,

878   Perlwitz, J., Basart, S., Di Tomaso, E., Escribano, J., MacChia, F., Montané, G., Mahowald, N.

879   M., Green, R. O., Thompson, D. R., and Pérez García-Pando, C.: Modeling dust mineralogical

880   composition: sensitivity to soil mineralogy atlases and their expected climate impacts, Atmos.

881   Chem. Phys., 23, 8623–8657, https://doi.org/10.5194/acp-23-8623-2023, 2023.

882   Green, R. O., Mahowald, N., Ung, C., Thompson, D. R., Bator, L., Bennet, M., Bernas, M.,

883   Blackway, N., Bradley, C., Cha, J., Clark, P., Clark, R., Cloud, D., Diaz, E., Ben Dor, E., Duren,

884   R., Eastwood, M., Ehlmann, B. L., Fuentes, L., Ginoux, P., Gross, J., He, Y., Kalashnikova, O.,

885   Kert, W., Keymeulen, D., Klimesh, M., Ku, D., Kwong-Fu, H., Liggett, E., Li, L., Lundeen, S.,

886 Makowski, M. D., Mazer, A., Miller, R., Mouroulis, P., Oaida, B., Okin, G. S., Ortega, A., Oyake,
887 A., Nguyen, H., Pace, T., Painter, T. H., Pempejian, J., Garcia-Pando, C. P., Pham, T., Phillips, B.,
888 Pollock, R., Purcell, R., Realmuto, V., Schoolcraft, J., Sen, A., Shin, S., Shaw, L., Soriano, M.,
889 Swayze, G., Thingvold, E., Vaid, A., and Zan, J.: The Earth Surface Mineral Dust Source
890 Investigation: An Earth Science Imaging Spectroscopy Mission, in: 2020 IEEE Aerospace
891 Conference, 1–15, https://doi.org/10.1109/AERO47225.2020.9172731, 2020.

892 Grider, A., Ponette-González, A., and Heindel, R.: Calcium and ammonium now control the pH
893 of wet and bulk deposition in Ohio, U.S., Atmos. Environ., 310,
894 https://doi.org/10.1016/j.atmosenv.2023.119986, 2023.

895 Guo, H., Ming, Y., Fan, S., Zhou, L., Harris, L., and Zhao, M.: Two-Moment Bulk Cloud
896 Microphysics With Prognostic Precipitation in GFDL's Atmosphere Model AM4.0: Configuration
897 and Performance, J. Adv. Model. Earth Syst., 13, https://doi.org/10.1029/2020MS002453, 2021.

898 Harris, I., Osborn, T. J., Jones, P., and Lister, D.: Version 4 of the CRU TS monthly high-resolution
899 gridded multivariate climate dataset, Sci. Data, 7, https://doi.org/10.1038/s41597-020-0453-3,
900 2020.

901 Harrison, A. D., Lever, K., Sanchez-Marroquin, A., Holden, M. A., Whale, T. F., Tarn, M. D.,
902 McQuaid, J. B., and Murray, B. J.: The ice-nucleating ability of quartz immersed in water and its
903 atmospheric importance compared to K-feldspar, Atmos. Chem. Phys., 19, 11343–11361,
904 https://doi.org/10.5194/acp-19-11343-2019, 2019.

905 Huang, Y., Kok, J. F., Saito, M., and Muñoz, O.: Single-scattering properties of ellipsoidal dust
906 aerosols constrained by measured dust shape distributions, Atmos. Chem. Phys., 23, 2557–2577,
907 https://doi.org/10.5194/acp-23-2557-2023, 2023.

908 Huneeus, N., Schulz, M., Balkanski, Y., Griesfeller, J., Prospero, J., Kinne, S., Bauer, S., Boucher,
909 O., Chin, M., Dentener, F., Diehl, T., Easter, R., Fillmore, D., Ghan, S., Ginoux, P., Grini, A.,
910 Horowitz, L., Koch, D., Krol, M. C., Landing, W., Liu, X., Mahowald, N., Miller, R., Morcrette,
911 J. J., Myhre, G., Penner, J., Perlwitz, J., Stier, P., Takemura, T., and Zender, C. S.: Global dust
912 model intercomparison in AeroCom phase i, Atmos. Chem. Phys., 11, 7781–7816,
913 https://doi.org/10.5194/acp-11-7781-2011, 2011.

914 Jordan, A. K., Gnanadesikan, A., and Zaitchik, B.: Simulated dust aerosol impacts on western

915   sahelian rainfall: Importance of ocean coupling, J. Clim., 31, 9107–9124,
916   https://doi.org/10.1175/JCLI-D-17-0819.1, 2018.

917   Journet, E., Balkanski, Y., and Harrison, S. P.: A new data set of soil mineralogy for dust-cycle
918   modeling, Atmos. Chem. Phys., 14, 3801–3816, https://doi.org/10.5194/acp-14-3801-2014, 2014.

919   Kelly, J. T., Chuang, C. C., and Wexler, A. S.: Influence of dust composition on cloud droplet
920   formation, Atmos. Environ., 41, 2904–2916, https://doi.org/10.1016/j.atmosenv.2006.12.008,
921   2007.

922   Kok, J. F.: A scaling theory for the size distribution of emitted dust aerosols suggests climate
923   models underestimate the size of the global dust cycle, Proc. Natl. Acad. Sci. U. S. A., 108, 1016–
924   1021, https://doi.org/10.1073/pnas.1014798108, 2011.

925   Kok, J. F., Ridley, D. A., Zhou, Q., Miller, R. L., Zhao, C., Heald, C. L., Ward, D. S., Albani, S.,
926   and Haustein, K.: Smaller desert dust cooling effect estimated from analysis of dust size and
927   abundance, Nat. Geosci., 10, 274–278, https://doi.org/10.1038/Ngeo2912, 2017.

928   Lau, K. M., Kim, K. M., Sud, Y. C., and Walker, G. K.: A GCM study of the response of the
929   atmospheric water cycle of West Africa and the Atlantic to Saharan dust radiative forcing, Ann.
930   Geophys., 27, 4023–4037, https://doi.org/10.5194/angeo-27-4023-2009, 2009.

931   Li, L., Mahowald, N. M., Miller, R. L., Pérez Garciá-Pando, C., Klose, M., Hamilton, D. S.,
932   Gonçalves Ageitos, M., Ginoux, P., Balkanski, Y., Green, R. O., Kalashnikova, O., Kok, J. F.,
933   Obiso, V., Paynter, D., and Thompson, D. R.: Quantifying the range of the dust direct radiative
934   effect due to source mineralogy uncertainty, Atmos. Chem. Phys., 21, 3973–4005,
935   https://doi.org/10.5194/acp-21-3973-2021, 2021.

936   Loeb, N. G., Doelling, D. R., Wang, H., Su, W., Nguyen, C., Corbett, J. G., Liang, L., Mitrescu,
937   C., Rose, F. G., and Kato, S.: Clouds and the Earth'S Radiant Energy System (CERES) Energy
938   Balanced and Filled (EBAF) top-of-atmosphere (TOA) edition-4.0 data product, J. Clim., 31, 895–
939   918, https://doi.org/10.1175/JCLI-D-17-0208.1, 2018.

940   Mahowald, N.: Aerosol indirect effect on biogeochemical cycles and climate, Science (80-.)., 334,
941   794–796, https://doi.org/10.1126/science.1207374, 2011.

942   Matthes, K., Funke, B., Andersson, M. E., Barnard, L., Beer, J., Charbonneau, P., Clilverd, M. A.,
943   Dudok De Wit, T., Haberreiter, M., Hendry, A., Jackman, C. H., Kretzschmar, M., Kruschke, T.,

944 Kunze, M., Langematz, U., Marsh, D. R., Maycock, A. C., Misios, S., Rodger, C. J., Scaife, A. A.,
945 Seppälä, A., Shangguan, M., Sinnhuber, M., Tourpali, K., Usoskin, I., Van De Kamp, M.,
946 Verronen, P. T., and Versick, S.: Solar forcing for CMIP6 (v3.2), Geosci. Model Dev., 10, 2247–
947 2302, https://doi.org/10.5194/gmd-10-2247-2017, 2017.

948 Meinshausen, M., Vogel, E., Nauels, A., Lorbacher, K., Meinshausen, N., Etheridge, D. M., Fraser,
949 P. J., Montzka, S. A., Rayner, P. J., Trudinger, C. M., Krummel, P. B., Beyerle, U., Canadell, J.
950 G., Daniel, J. S., Enting, I. G., Law, R. M., Lunder, C. R., O'Doherty, S., Prinn, R. G., Reimann,
951 S., Rubino, M., Velders, G. J. M., Vollmer, M. K., Wang, R. H. J., and Weiss, R.: Historical
952 greenhouse gas concentrations for climate modelling (CMIP6), Geosci. Model Dev., 10, 2057–
953 2116, https://doi.org/10.5194/gmd-10-2057-2017, 2017.

954 Miller, R. L. and Tegen, I.: Climate response to soil dust aerosols, J. Clim., 11, 3247–3267,
955 https://doi.org/10.1175/1520-0442(1998)011<3247:CRTSDA>2.0.CO;2, 1998.

956 Miller, R. L., Perlwitz, J., and Tegen, I.: Feedback upon dust emission by dust radiative forcing
957 through the planetary boundary layer, J. Geophys. Res. D Atmos., 109, 1–17,
958 https://doi.org/10.1029/2004JD004912, 2004.

959 Miller, R. L., Knippertz, P., Pérez García-Pando, C., Perlwitz, J. P., and Tegen, I.: Impact of dust
960 radiative forcing upon climate, in: Mineral Dust: A Key Player in the Earth System, Springer
961 Netherlands, 327–357, https://doi.org/10.1007/978-94-017-8978-3_13, 2014.

962 Ming, Y., Ramaswamy, V., and Persad, G.: Two opposing effects of absorbing aerosols on global-
963 mean precipitation, Geophys. Res. Lett., 37, https://doi.org/10.1029/2010GL042895, 2010.

964 Obiso, V., Gonçalves Ageitos, M., Pérez García-Pando, C., Schuster, G. L., Bauer, S. E., Biagio,
965 C. Di, Formenti, P., Perlwitz, J. P., Tsigaridis, K., and Miller, R. L.: Observationally constrained
966 regional variations of shortwave absorption by iron oxides emphasize the cooling effect of dust,
967 https://doi.org/10.5194/egusphere-2023-1166, 2023.

968 Ocko, I. B., Ramaswamy, V., and Ming, Y.: Contrasting climate responses to the scattering and
969 absorbing features of anthropogenic aerosol forcings, J. Clim., 27, 5329–5345,
970 https://doi.org/10.1175/JCLI-D-13-00401.1, 2014.

971 Panta, A., Kandler, K., Alastuey, A., González-Flórez, C., González-Romero, A., Klose, M.,
972 Querol, X., Reche, C., Yus-Díez, J., and Pérez García-Pando, C.: Insights into the single-particle

973   composition, size, mixing state, and aspect ratio of freshly emitted mineral dust from field

974   measurements in the Moroccan Sahara using electron microscopy, Atmos. Chem. Phys., 23, 3861–

975   3885, https://doi.org/10.5194/acp-23-3861-2023, 2023.

976   Paulot, F., Ginoux, P., Cooke, W. F., Donner, L. J., Fan, S., Lin, M. Y., Mao, J., Naik, V., and

977   Horowitz, L. W.: Sensitivity of nitrate aerosols to ammonia emissions and to nitrate chemistry:

978   Implications for present and future nitrate optical depth, Atmos. Chem. Phys., 16, 1459–1477,

979   https://doi.org/10.5194/acp-16-1459-2016, 2016.

980   Pérez, C., Nickovic, S., Pejanovic, G., Baldasano, J. M., and Özsoy, E.: Interactive dust-radiation

981   modeling: A step to improve weather forecasts, J. Geophys. Res. Atmos., 111,

982   https://doi.org/10.1029/2005JD006717, 2006.

983   Persad, G. G., Ming, Y., and Ramaswamy, V.: The role of aerosol absorption in driving clear-sky

984   solar dimming over East Asia, J. Geophys. Res., 119, 10,410-10,424,

985   https://doi.org/10.1002/2014JD021577, 2014.

986   Réveillet, M., Dumont, M., Gascoin, S., Lafaysse, M., Nabat, P., Ribes, A., Nheili, R., Tuzet, F.,

987   Ménégoz, M., Morin, S., Picard, G., and Ginoux, P.: Black carbon and dust alter the response of

988   mountain snow cover under climate change, Nat. Commun., 13, https://doi.org/10.1038/s41467-

989   022-32501-y, 2022.

990   Rosenfeld, D., Rudich, Y., and Lahav, R.: Desert dust suppressing precipitation: A possible

991   desertification feedback loop, Proc. Natl. Acad. Sci. U. S. A., 98, 5975–5980,

992   https://doi.org/10.1073/pnas.101122798, 2001.

993   Ryder, C. L., Marenco, F., Brooke, J. K., Estelles, V., Cotton, R., Formenti, P., McQuaid, J. B.,

994   Price, H. C., Liu, D., Ausset, P., Rosenberg, P. D., Taylor, J. W., Choularton, T., Bower, K., Coe,

995   H., Gallagher, M., Crosier, J., Lloyd, G., Highwood, E. J., and Murray, B. J.: Coarse-mode mineral

996   dust size distributions, composition and optical properties from AER-D aircraft measurements

997   over the tropical eastern Atlantic, Atmos. Chem. Phys., 18, 17225–17257,

998   https://doi.org/10.5194/acp-18-17225-2018, 2018.

999   Scanza, R. A., Mahowald, N., Ghan, S., Zender, C. S., Kok, J. F., Liu, X., Zhang, Y., and Albani,

1000   S.: Modeling dust as component minerals in the Community Atmosphere Model: Development of

1001   framework and impact on radiative forcing, Atmos. Chem. Phys., 15, 537–561,

1002   https://doi.org/10.5194/acp-15-537-2015, 2015.

1003   Schuster, G. L., Dubovik, O., and Arola, A.: Remote sensing of soot carbon - Part 1: Distinguishing
1004   different absorbing aerosol species, Atmos. Chem. Phys., 16, 1565–1585,
1005   https://doi.org/10.5194/acp-16-1565-2016, 2016.

1006   Sinyuk, A., Sinyuk, A., Holben, B. N., Eck, T. F., Eck, T. F., M. Giles, D., M. Giles, D., Slutsker,
1007   I., Slutsker, I., Korkin, S., Korkin, S., S. Schafer, J., S. Schafer, J., Smirnov, A., Smirnov, A.,
1008   Sorokin, M., Sorokin, M., and Lyapustin, A.: The AERONET Version 3 aerosol retrieval algorithm,
1009   associated uncertainties and comparisons to Version 2, Atmos. Meas. Tech., 13, 3375–3411,
1010   https://doi.org/10.5194/amt-13-3375-2020, 2020.

1011   Skiles, S. M. K., Flanner, M., Cook, J. M., Dumont, M., and Painter, T. H.: Radiative forcing by
1012   light-absorbing particles in snow, https://doi.org/10.1038/s41558-018-0296-5, 1 November 2018.

1013   Sokolik, I. N. and Toon, O. B.: Incorporation of mineralogical composition into models of the
1014   radiative properties of mineral aerosol from UV to IR wavelengths, J. Geophys. Res., 104, 9423–
1015   9444, https://doi.org/Doi 10.1029/1998jd200048, 1999.

1016   Song, C. H. and Carmichael, G. R.: Gas-particle partitioning of nitric acid modulated by alkaline
1017   aerosol, J. Atmos. Chem., 40, 1–22, https://doi.org/10.1023/A:1010657929716, 2001.

1018   Song, Q., Zhang, Z., Yu, H., Kok, J. F., Di Biagio, C., Albani, S., Zheng, J., and Ding, J.: Size-
1019   resolved dust direct radiative effect efficiency derived from satellite observations, Atmos. Chem.
1020   Phys., 22, 13115–13135, https://doi.org/10.5194/acp-22-13115-2022, 2022.

1021   Strong, J. D. O., Vecchi, G. A., and Ginoux, P.: The response of the tropical Atlantic and West
1022   African climate to Saharan dust in a fully coupled GCM, J. Clim., 28, 7071–7092,
1023   https://doi.org/10.1175/JCLI-D-14-00797.1, 2015.

1024   Strong, J. D. O., Vecchi, G. A., and Ginoux, P.: The Climatological Effect of Saharan Dust on
1025   Global Tropical Cyclones in a Fully Coupled GCM, J. Geophys. Res. Atmos., 123, 5538–5559,
1026   https://doi.org/10.1029/2017JD027808, 2018.

1027   Taylor, K. E., Williamson, D., and Zwiers, F.: The sea surface temperature and sea-ice
1028   concentration boundary conditions for AMIP II simulations, Program for Climate Model
1029   Diagnosis and Intercomparison, Lawrence Livermore …, 2000.

1030   Zender, C. S., Newman, D., and Torres, O.: Spatial heterogeneity in aeolian erodibility: Uniform,
1031   topographic, geomorphic, and hydrologic hypotheses, J. Geophys. Res. Atmos., 108,
1032   https://doi.org/10.1029/2002jd003039, 2003.

1033   Zhang, X. L., Wu, G. J., Zhang, C. L., Xu, T. L., and Zhou, Q. Q.: What is the real role of iron
1034   oxides in the optical properties of dust aerosols?, Atmos. Chem. Phys., 15, 12159–12177,
1035   https://doi.org/10.5194/acp-15-12159-2015, 2015.

1036   Zhao, M., Golaz, J. C., Held, I. M., Guo, H., Balaji, V., Benson, R., Chen, J. H., Chen, X., Donner,
1037   L. J., Dunne, J. P., Dunne, K., Durachta, J., Fan, S. M., Freidenreich, S. M., Garner, S. T., Ginoux,
1038   P., Harris, L. M., Horowitz, L. W., Krasting, J. P., Langenhorst, A. R., Liang, Z., Lin, P., Lin, S.
1039   J., Malyshev, S. L., Mason, E., Milly, P. C. D., Ming, Y., Naik, V., Paulot, F., Paynter, D., Phillipps,
1040   P., Radhakrishnan, A., Ramaswamy, V., Robinson, T., Schwarzkopf, D., Seman, C. J.,
1041   Shevliakova, E., Shen, Z., Shin, H., Silvers, L. G., Wilson, J. R., Winton, M., Wittenberg, A. T.,
1042   Wyman, B., and Xiang, B.: The GFDL Global Atmosphere and Land Model AM4.0/LM4.0: 1.
1043   Simulation Characteristics With Prescribed SSTs, J. Adv. Model. Earth Syst., 10, 691–734,
1044   https://doi.org/10.1002/2017MS001208, 2018a.

1045   Zhao, M., Golaz, J. C., Held, I. M., Guo, H., Balaji, V., Benson, R., Chen, J. H., Chen, X., Donner,
1046   L. J., Dunne, J. P., Dunne, K., Durachta, J., Fan, S. M., Freidenreich, S. M., Garner, S. T., Ginoux,
1047   P., Harris, L. M., Horowitz, L. W., Krasting, J. P., Langenhorst, A. R., Liang, Z., Lin, P., Lin, S.
1048   J., Malyshev, S. L., Mason, E., Milly, P. C. D., Ming, Y., Naik, V., Paulot, F., Paynter, D., Phillipps,
1049   P., Radhakrishnan, A., Ramaswamy, V., Robinson, T., Schwarzkopf, D., Seman, C. J.,
1050   Shevliakova, E., Shen, Z., Shin, H., Silvers, L. G., Wilson, J. R., Winton, M., Wittenberg, A. T.,
1051   Wyman, B., and Xiang, B.: The GFDL Global Atmosphere and Land Model AM4.0/LM4.0: 2.
1052   Model Description, Sensitivity Studies, and Tuning Strategies, J. Adv. Model. Earth Syst., 10,
1053   735–769, https://doi.org/10.1002/2017MS001209, 2018b.

1054   Paul Ginoux, María Gonçalves Ageitos, Qianqian Song, Ronald L Miller, Vincenzo Obiso, and
1055   Carlos Pérez García-Pando (2023), Implementation of dust mineralogy in the GFDL AM4.0
1056   climate model, in preparation.

1057